HHS Public Access

Author manuscript

Cancer Res. Author manuscript; available in PMC 2024 August 15.

Published in final edited form as:

Cancer Res. 2024 February 15; 84(4): 577–597. doi:10.1158/0008-5472.CAN-23-3239.

R-loop accumulation in spliceosome mutant leukemias confers sensitivity to PARP1 inhibition by triggering transcription-replication conflicts

Zhiyan Silvia Liu[1,3,23], **Sayantani Sinha**[2,23], **Maxwell Bannister**[3], **Axia Song**[2], **Erica Arriaga-Gomez**[2], **Alexander J. McKeeken**[3,4], **Elizabeth A. Bonner**[2,5], **Benjamin K. Hanson**[3,6], **Martina Sarchi**[7,8], **Kouhei Takashima**[9,10,11], **Dawei Zong**[1,3], **Victor M. Corral**[1,3], **Evan Nguyen**[2], **Jennifer Yoo**[3], **Wannasiri Chiraphapphaiboon**[3], **Cassandra Leibson**[3], **Matthew C. McMahon**[1,3], **Sumit Rai**[12], **Elizabeth M. Swisher**[13], **Zohar Sachs**[3,14], **Srinivas Chatla**[15], **Derek L. Stirewalt**[2,16], **H. Joachim Deeg**[16], **Tomasz Skorski**[15,17], **Eirini P. Papapetrou**[9,10,11], **Matthew J. Walter**[18], **Timothy A. Graubert**[12], **Sergei Doulatov**[7,19,20], **Stanley C. Lee**[2,21,24], **Hai Dang Nguyen**[3,22,24]

[1]Molecular Pharmacology and Therapeutics Graduate Program, Department of Pharmacology, University of Minnesota, Minneapolis, MN, USA

[2]Translational Science and Therapeutics Division, Fred Hutchinson Cancer Center, Seattle, WA, USA

[3]Masonic Cancer Center, University of Minnesota, Minneapolis, MN, USA

[4]Bioinformatics and Computational Biology Program, University of Minnesota, Minneapolis, MN, USA

[5]Molecular and Cellular Biology Graduate Program, University of Washington, Seattle, WA, USA

[6]Department of Biochemistry, Molecular Biology, and Biophysics Graduate Program, University of Minnesota, Minneapolis, MN, USA

[7]Division of Hematology and Oncology, Department of Medicine, University of Washington, Seattle, WA, USA

[8]Department of Molecular Medicine, University of Pavia, 27100 Pavia PV, Italy

[9]Department of Oncological Sciences, Tisch Cancer Institute, Icahn School of Medicine at Mount Sinai, New York, NY, USA

[10]Institute for Regenerative Medicine and Black Family Stem Cell Institute, Icahn School of Medicine at Mount Sinai, New York, NY, USA

[11]Center for Advancement of Blood Cancer Therapies, Icahn School of Medicine at Mount Sinai, New York, NY, USA

[24] Corresponding authors: Stanley C. Lee, Translational Science and Therapeutics Division, Fred Hutchinson Cancer Center, Seattle, WA 98109, USA; sclee3@fredhutch.org, Hai Dang Nguyen, Department of Pharmacology, Masonic Cancer Center, University of Minnesota, MN 55455, USA; hdnguyen@umn.edu.

Additional Information: Spouse of T.A.G is an employee of Alexion (owned by AstraZeneca) and holds equity in AZ. Other authors have no conflict of interest to declare with respect to the studies or results presented in this manuscript. K.T is an employee of Daiichi Sankyo Co., Ltd.

[12]Massachusetts General Hospital Cancer Center, Charlestown, MA

[13]Division of Gynecologic Oncology, Department of Obstetrics and Gynecology, University of Washington School of Medicine, Seattle, WA 98195

[14]Division of Hematology, Oncology, and Transplantation, Department of Medicine, University of Minnesota, Minneapolis, MN, USA

[15]Fels Cancer Institute for Personalized Medicine, Lewis Katz School of Medicine, Temple University, Philadelphia, PA 19140, USA

[16]Clinical Research Division, Fred Hutchinson Cancer Center, Seattle, WA, USA

[17]Department of Cancer and Cellular Biology, Lewis Katz School of Medicine, Temple University, Philadelphia, PA 19140, USA

[18]Division of Oncology, Department of Internal Medicine, Washington University School of Medicine, St Louis, MO, USA

[19]Department of Genome Sciences, University of Washington, Seattle, WA, USA

[20]Institute of Stem Cell and Regenerative Medicine, University of Washington, Seattle, WA, USA

[21]Department of Laboratory Medicine & Pathology, University of Washington, Seattle, WA, USA

[22]Department of Pharmacology, University of Minnesota, Minneapolis, MN, USA

[23]These authors contributed equally.

Abstract

RNA splicing factor (SF) gene mutations are commonly observed in patients with myeloid malignancies. Here we showed that *SRSF2*- and *U2AF1*-mutant leukemias are preferentially sensitive to PARP inhibitors (PARPi) despite being proficient in homologous recombination repair. Instead, SF-mutant leukemias exhibited R-loop accumulation that elicited an R-loop associated PARP1 response, rendering cells dependent on PARP1 activity for survival. Consequently, PARPi induced DNA damage and cell death in SF-mutant leukemias in an R-loop dependent manner. PARPi further increased aberrant R-loop levels, causing higher transcription-replication collisions and triggering ATR activation in SF-mutant leukemias. Ultimately, PARPi-induced DNA damage and cell death in SF-mutant leukemias could be enhanced by ATR inhibition. Finally, the level of PARP1 activity at R loops correlated with PARPi sensitivity, suggesting that R-loop associated PARP1 activity could be predictive of PARPi sensitivity in patients harboring SF gene mutations. This study highlights the potential of targeting different R-loop response pathways caused by spliceosome gene mutations as a therapeutic strategy for treating cancer.

INTRODUCTION

Somatic mutations in RNA splicing factors (SF) *SF3B1*, *SRSF2*, *U2AF1* and *ZRSR2* are recurrently observed in patients with hematologic malignancies, highlighting the role of splicing dysregulation in oncogenic transformation (1,2). These mutations are typically acquired as early mutational events in disease etiology and are enriched across a spectrum of clonal myeloid disorders including clonal hematopoiesis (CH) (3–6), myelodysplastic

syndromes (MDS) (7–9), chronic myelomonocytic leukemia (CMML) (10), and secondary acute myeloid leukemia (sAML) (11). Except for *SF3B1*-mutant MDS with refractory anemia and ring sideroblasts (MDS-RARS), patients carrying SF mutations are often associated with poor prognosis and increased likelihood of leukemic transformation (11).

Mutations in *SF3B1*, *SRSF2* and *U2AF1* occur as missense mutations at specific amino acid residues that confer neomorphic functions. In contrast, *ZRSR2* is subjected to nonsense or frameshift mutations across the coding region and these alterations are predicted to result in loss of function (11). Extensive transcriptomic analyses have shown that spliceosome mutations cause widespread splicing abnormalities by altering the use of canonical splice site choices. While many aberrantly spliced transcripts have been associated with spliceosome mutations, only a handful of events have been functionally linked to disease phenotype. This raises the possibility that in addition to splicing abnormalities, splicing-independent mechanisms may also contribute to the development of myeloid neoplasms. Indeed, multiple studies have identified abnormal accumulation of R-loops as a shared molecular consequence downstream of spliceosome gene mutations (12–16). R-loops are transcription intermediates that contain an RNA:DNA hybrid structure and a displaced single-stranded DNA (ssDNA) (17). Under homeostatic conditions, R-loops are tightly regulated to preserve genome stability. This is orchestrated by different mechanisms that prevent nascent RNA from hybridizing to DNA, alleviate RNA polymerase pausing, or physically remove RNA from RNA:DNA hybrids (17,18). However, when R-loops are aberrantly accumulated and/or distributed in the genome, especially at sites of transcription-replication fork collisions, they can cause increased genomic instability and ultimately cell death. Although the causal link between R-loop dysregulation and disease etiology remains to be formally established, cancers with aberrant R-loop accumulation may become addicted to specific R-loop tolerance response for survival.

There have been extensive efforts to therapeutically target RNA splicing in cancers. One general approach involves targeting the core spliceosome based on observations that SF-mutant cells are dependent on optimal splicing activity for survival (19–22). Indeed, preclinical studies using pharmacologic inhibitors targeting the U2 small nuclear ribonucleoprotein (U2 snRNP) complex (e.g. E7107, H3B-8800) and splicing regulator proteins (e.g. PRMT1/5, RBM39) have shown preferential killing of SF-mutant leukemias *in vivo* (19,20,23–26). However, data from a recent phase-I clinical trial of H3B-8800 in spliceosome-mutant MDS and CMML patients showed minimal clinical response, highlighting the need to identify additional therapeutic modalities (27). Consistent with this notion, RNA splicing perturbation, by either genetic or pharmacologic approaches, activates the ATR, but not ATM, kinase signaling pathway that are critical for survival in an R-loop-dependent manner (13,14). Based on the promising preclinical data, a Phase I/II clinical trial using ATR inhibitor, AZD6738, is currently testing this approach in spliceosome-mutant MDS and CMML patients (28). This proof-of-principle study highlights that targeting R-loop response pathways could emerge as a potential therapeutic strategy in this genetically defined subset of myeloid malignancies.

The association between RNA splicing perturbation, R-loop accumulation, and genomic instability prompted us to identify novel regulators of R-loop response pathways that are

critical for survival of SF-mutant leukemia. Here, we report that leukemia cells carrying spliceosome mutations elicited a poly-ADP-ribose polymerase 1 (PARP1) response at R-loops. SRSF2- and U2AF1-mutant cancer cells were preferentially sensitive to a panel of PARP inhibitors and this sensitivity was driven, in part, via an R-loop-dependent mechanism instead of defective homologous recombination (HR) repair. PARP inhibition further induced aberrant accumulation of R loops, leading to collisions between RNA polymerase II and DNA replisome. The transcription-replication conflict, in turn, activates ATR signaling, rendering cells more dependent on ATR activity for survival. Consequently, combined PARP and ATR inhibition increased DNA damage and cell death in SF-mutant leukemic cells. Finally, expression of the R-loop resolving endonuclease RNase H1 attenuated the induced DNA damage caused by PARPi+ATRi in spliceosome mutant cells, suggesting that the DNA damage induced by PARP+ATR inhibitors arises from R loops. These results highlight that PARP1 plays an important role in suppressing R-loop-associated genomic instability in spliceosome mutant cells. Lastly, combined PARP and ATR inhibition resulted in synergistic killing of SF-mutant leukemias *ex vivo* and significantly reduced leukemia burden *in vivo*. Notably, the levels of R-loop-associated PARP1 activity correlated with PARPi-induced cell death in a panel of primary AML patient cells harboring SF mutations. Taken together, our data establish a previously unknown link between R-loop-induced PARP1 activation and RNA splicing perturbation and provide a mechanistic rationale to evaluate the clinical efficacy of PARP inhibitors in spliceosome-mutant malignancies. Furthermore, our study highlights a new therapeutic potential of targeting R-loop response pathway(s) caused by different spliceosome gene mutations.

MATERIALS AND METHODS

Antibodies, oligos, and plasmids

All antibody information is available in Supplementary Table S1. All primers and plasmids used in this study are available in Supplementary Tables S2 and S3, respectively.

Cell culture

MLL-AF9, K562, U937, OCI-AML3, HL60, THP1, K052, NKM1, HNT34, 293T and GP-II cells were maintained in base media (RPMI or IMDM) supplemented with penicillin-streptomycin (100 U/mL, Gibco #15140122), GlutaMax (1%, Gibco #35050061), sodium pyruvate (1 mM, Gibco #11360070) and non-essential amino acids (1%, Gibco #11140050) and maintained in a 37°C/5% CO_2 incubator. 293T (Clontech), GP2–293 (Clontech), HeLa cells (obtained from Zou laboratory) and all their derived cell lines were previously reported (21) and were maintained in DMEM supplemented with 10% or 20% heat-inactivated FBS. The HeLa cells have been analyzed by RNA-seq. The K562 cells were previously obtained from ATCC and have been analyzed by RNA-seq. Various leukemia cell lines were purchased from ATCC and DSMZ without further authentication. Cell lines used in this study were tested for *Mycoplasma* and passaged for less than 2 months after thawing.

To introduce *U2AF1-S34F* mutation at the endogenous locus, K562 cells from ATCC (CCL-243), were resuspended in Buffer R (Thermo Fisher Scientific) and gently mixed with the freshly prepared Hifi2-Cas9 (MCLAB) – gRNA (Synthego) ribonucleoprotein

complex including a single stranded donor oligodeoxynucleotide (ssODN) repair template and electroporated using the Neon Electroporation System (Thermo Fisher Scientific) as previously described (29). The oligonucleotides sequences used for gene editing are available in Supplementary Table S2. Clonal lines were expanded by limiting dilution and confirmed to harbor the desired substitution and zygosity by amplicon-based next-generation sequencing. Isogenic U2AF1-wildtype clones were prepared and isolated under identical conditions. K562 parental, K562 SRSF2^{P95H}, K562 SF3B1^{K700E} (17) and K562 U2AF1^{S34F} isogenic cell lines were cultured in IMDM/10% heat-inactivated FBS. To generate *MLL-AF9* murine leukemia cell lines, primary leukemic cells were harvested from the bone marrow (BM) of moribund mice and adapted to liquid culture in IMDM/10% FBS supplemented with recombinant mouse (rm) IL-3 (5 ng/mL) and rmSCF (10 ng/mL) for at least 2 weeks. For colony forming assays, *MLL-AF9* murine leukemia cells were cultured in MethoCult™ (M3231, StemCell Technologies) supplemented with penicillin-streptomycin (100 U/mL), rmIL3 (10 ng/mL) and rmSCF (20 ng/mL). Primary human AML cells were maintained in StemSpan SFEM-II media (StemCell Technologies) in the presence of penicillin-streptomycin (100 U/mL), with recombinant human (rh) SCF (50 ng/ml), rhFLT3L (50 ng/mL), rhTPO (50 ng/mL), rhIL3 (10 ng/mL) and rhIL6 (10 ng/mL). iPSC reprogramming, hematopoietic differentiation, and 5F-HPCs generation was performed as previously described (30,31). 5F-HPCs cells were cultured in SFEM (StemCell Technologies) with rhSCF (50 ng/mL), rhFLT3L (50 ng/mL), rhTPO (50 ng/mL), rhIL6 (50 ng/mL) rhIL-3 (10 ng/mL) and penicillin/streptomycin. Doxycycline was added at 2 μg/mL (Sigma). The WT iPSC N-2.12-D1-1 line was generated as previously described (32). The *SRSF2*P95L mutant and *U2AF1*S34F mutant iPSC lines were derived from N-2.12-D1-1 line by CRISPR/Cas9-mediated gene editing (33). Cells were maintained in iPSC culture media StemPro34 SFM with 1% nonessential amino acids (NEAA), L-glutamine (1 mmol/L) and β-mercaptoethanol (0.1 mmol/L), supplemented with rhSCF (100 ng/mL), rhFLT3L (20 ng/mL), rhTPO (20 ng/mL), and rhIL3 (40 ng/mL). All cytokines were purchased from PeproTech. The *SRSF2*^{P95H} and *U2AF1*^{S34F} mutations in *MLL-AF9* and K562 isogenic cells were routinely confirmed by Sanger sequencing of the cDNA at the beginning and end of each experiment (see Supplementary Table S2).

Primary human AML patient samples

Cryopreserved de-identified peripheral blood or bone marrow specimens were obtained from the Fred Hutchinson Cancer Center/University of Washington Hematopoietic Diseases Repository (FHCC/UW-HDR). As part of the FHCC/UW-HDR, patient specimens are collected and stored under the oversight of Fred Hutch Institution Review Office, and all participants provided written informed consent that adhered to the guidelines of 1975 Declaration of Helsinki. AML diagnosis for all the patients was confirmed using established guidelines at the time of diagnosis. Results from targeted genomic sequencing, FLT3 fragment analyses, flow immunophenotyping and cytogenetics were available for all patients from the FHCC/UW-HDR. See Supplementary Table S4 for detailed genetic information for each patient sample.

Lentivirus and retrovirus production and transduction

For production of lentiviral particles, 293T cells (Clontech) were co-transfected with packaging plasmids pVSVG (4 μg; Clontech) and psPAX2 (6 μg; Addgene #12260, RRID:Addgene_12260) along with expression plasmids (10 μg). For production of retroviral particles, GP2–293 cells (Clontech) were co-transfected with packaging plasmids pVSVG (5 μg; Clontech, RRID:Addgene_85140) and pCL-Eco/Gag-Pol (4 μg; Addgene #12371) along with retroviral expression plasmids (10 μg). Calcium phosphate transfection method was used to produce lentiviral and retroviral particles. The cell density was maintained at 70% of a 10 cm tissue culture plate at the time of transfection followed by media change 24 hours post transfection. Supernatants containing the viral particles were collected at 48 and 72 hours post transfection. Cells were transduced using spinoculation method in the presence of RetroNectin (32 μg/mL; Clontech #T100-B) and polybrene (4 μg/mL; Millipore #TR-1003-G).

Animals

All animal experiments were performed with approval by and in accordance with the guidelines of the Fred Hutchinson Cancer Research Center (FHCRC) Institutional Animal Care and Use Committees. Animal experiments were performed within the FHCRC Comparative Medicine facility, which is fully accredited by the Association for Assessment and Accreditation of Laboratory Animal Care (AAALAC) and complies with all United States Department of Agriculture (USDA), Public Health Services (PHS), Washington State and local area animal welfare regulations. All mice were housed in individually ventilated and HEPA-filtered microisolator cage environments using reusable, autoclaved cages. Rooms were maintained on a 12:12 light:dark cycle, at a temperature of 72°± 3°F and humidity 30–70%. The *Srsf2*$^{P95H/+}$ (strain #028376) (34), *U2af1*$^{S34F/+}$ (strain #032638) (35), *Vav*-iCre$^{Tg/+}$ (strain #008610) (36), *Mx1*-Cre$^{Tg/+}$ (strain #003556) (37) and B6.SJL *Ptprc*^{a} *Pepc* (CD45.1; strain #002014) mice were purchased from The Jackson Laboratory (JAX) and were maintained on a C57BL/6 background. Generation and genotyping of mice were performed as described previously. B6.SJL *Ptprc*^{a} *Pepc* (CD45.1) mice were used as transplant recipients and were acclimatized for at least 5 days before experimentation. CD45.1 recipient mice conditioned with either one dose of 450 cGy (sub-lethal irradiation) or two doses of 550 cGy (lethal irradiation, 3 hours between doses) using a cesium source mouse irradiator (Mark I series 30JL Shepherd irradiator). NOD-*Prkdc*^{scid}/*Il2rg*$^{-/-}$/Tg(CMV-KITLG,CSF2,IL3) (NSG-SGM3) mice were purchased from The Jackson laboratory (JAX) to generate primary human AML patient-derived xenograft (PDX) models.

Generation of *MLL-AF9* murine leukemia *in vivo*

BM HSPCs from *Vav*-iCre$^{Tg/+}$ *Srsf2*$^{+/+}$, *Vav*-iCre$^{Tg/+}$ *Srsf2*$^{P95H/+}$, *Mx1*-Cre$^{Tg/+}$ *U2af1*$^{+/+}$ and *Mx1*-Cre$^{Tg/+}$ *U2af1*$^{S34F/+}$ mice were used to generate *MLL-AF9* leukemia model *in vivo*. Mice on *Mx1*-Cre background were treated with 3 doses of polyinosinic:polycytidylic acid (pIpC; 12mg/kg/day; GE Healthcare) every other day and bone marrow cells were harvested 2 months later to generate leukemia *in vivo*. Briefly, c-Kit^{+} cells were enriched from freshly dissected BM by magnetic isolation using the mouse CD117 MicroBeads (Miltenyi Biotec, #130-019-224) according to manufacturer's instructions. The c-Kit^{+} cell

fraction was stained with a cocktail of antibodies to label hematopoietic stem and progenitor cells (HSPCs), which are defined as $B220^-$, $CD19^-$, $CD3^-$, $CD4^-$, $CD8a^-$, $NK1.1^-$, $CD11c^-$, $Mac1^-$, $Gr\text{-}1^-$, $Ter119^-$, $FceRIa^-$, $Sca\text{-}1^+$ $c\text{-}Kit^+$ $CD135^-$ (antibody information is available in Supplementary Table S1). BM HSPCs were purified by fluorescence activated cell sorting using a BD FACSymphony S6 Cell Sorter (BD Biosciences) and cultured overnight in IMDM media supplemented with 10% FBS, rmSCF (50 ng/mL), rmTPO (25 ng/mL), rmIL-3 (10 ng/mL). The next day, HSPCs were transduced with *MLL-AF9* retrovirus for 24 hours and cells were washed and allowed to rest overnight. The following day, *ex vivo* manipulated HSPCs together with 2×10^5 CD45.1 support BM cells were transplanted via intravenous tail vein injection into lethally irradiated CD45.1 recipients, and mice were monitored for leukemia development by visual inspection, peripheral blood donor cell chimerism by flow cytometry and complete blood count using the Element HT5 Automated Blood Analyzer (Heska Corporation).

In vitro drug screen and cell viability assay

A detailed list of inhibitors used in the drug screen is listed in Supplementary Table S5. Cells were treated with the indicated drugs for 72–96 hours over 10 concentrations. Isogenic *MLL-AF9* murine leukemia cells and K562 cells were seeded in white flat-well 96-well plates (Costar, Corning) at a density of 5,000 and 500 cells per well respectively. For primary AML patient samples, cells were pre-stimulated for 36 hours in StemSpan SFEM-II media (StemCell Technologies) in the presence of penicillin-streptomycin (100 U/mL) and supplemented with rhSCF (50 ng/mL), rhFLT3L (50 ng/mL), rhTPO (50 ng/mL), rhIL3 (10 ng/mL) and rhIL6 (10 ng/mL). The immunophenotype of each AML sample was determined by flow cytometry as described above. Prior to culturing, AML samples were depleted of $CD3^+$ T cells using human CD3 MicroBeads (Miltenyi Biotec, #130–050-101) if the T cell percentage was > 5%. Human AML cells were seeded at a density of 10,000 cells per well and were treated with PARPi (Olaparib) and ATRi (AZD6738) for 96 hours. 5F-HPCs and K562 isogenic cells were plated on 96-well tissue culture-treated plates at a density of 15,000 and 500 cells per 150 μL per well, respectively. Cells were treated with 0–1mM μM PARPi (olaparib, rucaparib), and 0–10 μM ATRi (AZD6738) for 7 days. For iPSC-HPCs, cells were seeded on white bottom 96-well plates at a density of 2500 cells per well in a total volume of 200 μL. Cells were treated with 0–1 mM PARPi (olaparib) for 72 hours. The proportion of viable cells with drug treatment was calculated relative to DMSO control. Cell viability was determined using CellTiterGlo (Promega) according to the manufacturer's instructions. A three-parameter nonlinear fit of log(inhibitor) versus response was performed in GraphPad Prism v7.0 (GraphPad Software, San Diego, CA; RRID:SCR_002798) to determine IC50 values.

High-throughput cell viability analysis from drug screen

As a metric for cell viability, luminescence was expressed relative to cells treated with the respective drug's solvents. 4-parameter logistic (4PL) dose-response curves were fitted and visualized using Prism 9 software with the upper asymptotes fixed at 1. High-throughput processing of drug-screen results was enabled in R with the 'drc' package (version 3.0–1) to similarly fit 4PL curves and extract the IC_{50} statistic (38). Integrating fitted 4PL curves yields the area under the curve (AUC), a robust metric for drug responses (39). Since

drug dose-response curves vary for different drugs used in the screen, log-transformed drug concentrations were used to normalize the AUC to effectively linearizes the scale of drug concentrations used. For example, a 2-fold change in sensitivity occurring in the μM range for one drug registers the same as another drug occurring in the nM range. Next, integration was carried out over a defined range of concentrations, rendering the metric insensitive to the very beginning and ends of the sloped portion of the 4PL model. The normalized AUCs were measured as soon as the first curve dropped below 90% viable and ended once the last curve dropped below 10% viable. The differential normalized AUC (ΔAUC) was expressed as "$AUC^{wildtype} - AUC^{mutant}$", such that positive values indicate greater drug sensitivity in the mutant cell population.

In vitro drug combination assay

MLL-AF9 murine leukemia cells, K562 cells and primary human AML blasts were seeded in white flat-well 96-well plates (Costar, Corning) at a density of 5,000, 500 and 10,000 cells per well, respectively. Primary AML cells were pre-stimulated after T cell (CD3+) depletion for 36 hours in StemSpan SFEM-II media (StemCell Technologies) in the presence of penicillin-streptomycin (100 U/mL) and supplemented with rhSCF (50 ng/ml), rhFLT3L (50 ng/mL), rhTPO (50 ng/mL), rhIL3 (10 ng/mL) and rhIL6 (10 ng/mL). Cells were seeded at the desired density on 200 μL per well respectively and were treated with combination of olaparib (0–5 μM) and AZD6738 (0–5 μM) for 96 hours. The proportion of viable cells with drug treatment was calculated relative to DMSO control. Cell viability was determined using CellTiterGlo (Promega) according to the manufacturer's instructions. SynergyFinder (v3) was used to calculate the synergistic effect (Loewe score) of the drug combination. For colony forming assay, *MLL-AF9 Srsf2*$^{+/+}$ and *MLL-AF9 Srsf2*$^{P95H/+}$ murine leukemia cells were seeded at a density of 500 cells per dish in MethoCult medium (Stem Cell Technology #M3231) supplemented with mIL3 (10 ng/mL) and mSCF (20 ng/mL) containing either vehicle (DMSO) or combination of olaparib (PARPi: 0–500 nM) and AZD6738 (ATRi: 0–500 nM). Colonies were enumerated after 7 days of incubation.

Immunoblots

All immunoblots experiments were performed as previously described with some modifications (40). Cells were resuspended and lysed in a lysis buffer (100 mM Tris at pH 6.8, 1% SDS) and boiled for 15 min. Protein concentrations were normalized using a Pierce BCA protein assay kit (Thermo Fisher Scientific 23227) and mixed 1:1 with 2× SDS-PAGE loading buffer (100 mM Tris at pH 6.8, 12% glycerol, 3.5% SDS, 0.2 M DTT). Samples were loaded on polyacrylamide gels and run at 100 V for 90 min. Proteins were transferred onto PVDF membranes for 1.5 hours at 250 mA. Membranes were then blocked in Tris-buffered saline with 0.05% Tween-20 (TBS-T) and 5% milk for 1 hour at room temperature. Membranes were then immunoblotted with primary antibodies overnight at 4°C. Antibodies are listed in Supplementary Table S1. Membranes were washed 3 times with TBS-T and incubated for 1 hour at room temperature with secondary antibodies conjugated to horseradish peroxidase. Membranes were washed three times for 10 min with TBS-T and an enhanced chemiluminescence (ECL Bio-Rad 1705061) substrate was applied. Signals were detected using a ChemiDoc imaging system (Bio-Rad) with ImageLab v6.0.1. software.

Immunofluorescence

K562 cells were plated on poly-L-lysine (Sigma-Aldrich, P4707) treated coverslips at 37°C for 30 minutes for optimal attachment. For measuring γH2AX and Rad51 loading, cells were fixed with ice-cold methanol for 20 minutes at −20°C. Subsequently, cells were permeabilized with 1x PBS containing 0.5% Triton X-100, and treated in blocking buffer (1x PBS, 3% BSA, 0.05% Tween-20, and 10% milk) prior to primary antibody incubation overnight at 4°C. After the incubation in primary antibody, cells were washed three times with 1x PBS containing 0.05% Tween-20 and incubated with respective secondary antibody (1:1000) for 1 hour at room temperature. To visualize nuclei, cells were stained with DAPI and washed in PBS before mounted. Coverslips were mounted using ProLong™ Gold Antifade Mountant (Invitrogen, P36930). Images were captured using a Leica DMi8 microscope (Leica Microsystems) and analyzed using ImageJ software (RRID:SCR_003070).

All immunofluorescence experiments involving S9.6 staining were performed as previously described (41). Briefly, for S9.6 staining in K562 cells, after proper attachment, cells were pre-extracted with CSK buffer containing 0.25% Triton X-100 for 5 minutes, then fixed with 3% paraformaldehyde/2%sucrose for 10 minutes on ice. Then cells were denatured with ice-cold methanol for 20 minutes at −20°C before treated with blocking buffer (1x PBS, 5% BSA, 0.05% Triton X-100). Cells were then incubated with S9.6 antibody (purified from the HB-8730 hybridoma cell line, 1 μg/μL, 1:500) overnight at 4°C. The slides were washed three times with the wash buffer (1× PBS + 0.1% Triton X-100) and subsequently incubated with mouse secondary antibody conjugated with Cy3 for 1 hour at room temperature. Cells were washed three times with the wash buffer and then stained with DAPI and mounted using ProLong™ Gold Antifade Mountant.

The S9.6 staining in HeLa cells was processed as previously described (12). HeLa cells were trypsinized then resuspended in hypotonic solution (75 mM KCl) prewarmed to 37°C while being agitated on a vortex at a low speed. Cells were then incubated at 37°C for 12 minutes. Then 5–6 drops of freshly made, ice-cold fixation solution (methanol/glacial acetic acid 3:1 ratio) were dropped into the tube while cells were on low-vortex rate. Cells were then pelleted at 1000 rpm for 5 minutes, and supernatant was aspirated down to 500 μL. In a drop-wise manner, 6 mL of the fixation solution was added to the cells while cells were on a low-speed vortex. Cells were fixed for 20 minutes and washed one more time with the fixation solution. Cells were palleted and resuspended to a higher concentration and dropped on a coverslide. Dried slides were blocked with blocking buffer (1× PBS, 5% BSA, 0.5% Triton X-100) for 1 hour at room temperature and S9.6 antibody (purified from the HB-8730 hybridoma cell line, 1 μg/μL, 1:500) was incubated overnight at 4°C. The slides were processed as described above the next day.

Proximity ligation assay (PLA)

AML patient-derived cell lines and primary AML patient cells were attached on poly-L-lysine treated coverslips, then cells were fixed with ice-cold methanol for 20 minutes at −20°C. MAR/PAR:S9.6 PLA assay was performed as described previously (41). Briefly, cells were permeabilized with 1x PBS containing 0.5% Triton X-100 and treated with

either RNase H (New England Biolabs) diluted 1:50 in RNase H buffer (New England Biolabs), or mock (RNase H buffer only). Coverslips were incubated at 37°C for 3 hours. Then coverslips were washed three times and treated with blocking buffer (1x PBS, 5% BSA, 0.05% Triton X-100) prior to primary antibody incubation overnight at 4°C. For Pol2-pS2:PCNA PLA assay (42) with K562 cells, cells were pre-extracted with CSK buffer containing 0.25% Triton X-100 for 5 minutes, then fixed with 3% paraformaldehyde/ 2%sucrose for 10 minutes on ice. cells were then denatured with ice-cold methanol for 20 minutes at −20°C before treated with blocking buffer (1x PBS, 5% BSA, 0.05% Triton X-100). Cells were then incubated with primary antibody overnight at 4°C. The PLA assay using Duolink® In Situ Red Starter Kit Mouse/Rabbit (Sigma, DUO92101) was performed the next day according to manufacturer protocol beginning from Step 3.

Quantitative imaging-based cytometry (QIBC)

EdU labeling was done using the Click-iT™ EdU Cell Proliferation Kit for Imaging (Invitrogen, C10337). K562 cells were pulsed with 10 μM EdU for 30 minutes on poly-L-lysine treated coverslips. Then cells were fixed, blocked, and treated with primary and secondary antibody as previously described. After the final wash after secondary antibody incubation, coverslips were incubated on Click-iT® reaction cocktail (following the manufacturer protocol) for 30 minutes at room temperature. Cells were washed three more times with the wash buffer and stained with DAPI and mounted using ProLong™ Gold Antifade Mountant. For cell cycle analysis, total DAPI intensity level and mean EdU intensity level were measured for each cell. Cells with positive EdU staining were sorted into S-phase, and EdU-negative cells were sorted into 1N and 2N based on the total DAPI intensity and classified into G1 and G2 phase, respectively.

Cell cycle analysis

For cell cycle analysis using propidium iodide (PI) 1×10^6 *MLL-AF9 Srsf2* $^{+/+}$ and *MLL-AF9 Srsf2* $^{P95H/+}$ leukemia cells were washed in ice-cold PBS and fixed using 1% paraformaldehyde (PFA). Fixation solution was removed, and cells were washed with ice-cold PBS before permeabilizing with 70% ethanol added dropwise while vortexing. Cells were kept at 4ºC overnight. Post incubation supernatant was removed and washed twice with ice cold PBS. The cells were resuspended in 200 μL of PI staining solution (1xPBS containing 100 μg/mL RNAse A and 25 μg/mL PI) and incubated at 37°C for 30 minutes. Data was acquired immediately on a BD FACSymphony analyzer (BD Biosciences).

Cas9/mClover-LMNA assay

1×10^6 of each SRSF2^{P95H}, U2AF1^{S34F}, and their respective wildtype K562 cells were collected and resuspended in Buffer R, and nucleofected with Cas9.EF1a-BFP.sgLMNA (1 μg, pHD043, Addgene #98971) and pCAGGS Donor mClover-LMNA (3 μg, pHD044, Addgene #98970, RRID:Addgene #127347) using the Neon Transfection System 10 μL kit (Voltage: 1450, Width: 10, Pulses: 3). Cells were seeded into a 6-well plate with 5 mL of fresh culture media. After 2 days, cells were collected, and the percentage of mClover-positive cells in BFP-positive cells were analyzed by flow cytometry. As a positive control, electroporated cells were treated with either DMSO or an ATR inhibitor (VE-821, 1 μM; Selleckchem) for 48 hours.

DR-GFP reporter assay

DR-GFP reporter cassette (43,44) containing restriction endonuclease cleavage site for I-Sec1 restriction enzyme in Green Fluorescent Protein (*GFP*) gene was digested using I-Sec1 enzyme (Thermo Fisher #ER1771) to generate DSB in the GFP sequence. 25 μg of reporter DNA was digested at 37°C for 3 hours and linearized DNA was purified by PCR clean up micro kit (Qiagen #28106). DNA concentration and purification were measured in NanoDrop machine. Linearized DNA after I-SceI enzymatic digestion was co-nucleofected with Red Fluorescent Protein (RFP) expressing plasmid (pDsRed2-N1) into K562 WT and K562 $SRSF2^{P95H}$ cells using Nucleofector Kit (Lonza #VCA-1003). The nucleofection was performed in Nucleofector® 2b Device (Lonza # AAB-1001). In details, 5 μg of linearized DR-GFP reporter 2.5 μg pDsRed2-N1 in one cuvette provided in the kit. After transfection, cells were maintained in original medium for 72 hours. Cells were analyzed by flow cytometry. The DSB repair activity, in which DSB repair restored expression of GFP, was calculated as a ratio between total restored GFP(+) cells/total transfected RFP(+) cells or by percentage of total GFP+ cells/total RFP+ cells.

Apoptosis assay

To study PARPi-mediated cell apoptosis, 3×10^5 cells were subjected to olaparib treatment for 24 hours. Cells were harvested, washed twice with cold PBS, and resuspended in Annexin V binding buffer at a concentration of 1×10^6 cells/mL. Cells were incubated in Annexin V binding buffer (BD Biosciences, #556454) containing 5 μL of APC-conjugated Annexin V (BD Biosciences, #550475) per reaction and 2 μg/mL of propidium iodide (Sigma Aldrich, P4170). Cells were vortexed gently and incubated at room temperature in the dark for 15 minutes. Post incubation, 1x Annexin V binding buffer was added to each tube and samples were analyzed within 1 hour on a BD FACSymphony analyzer (BD Biosciences). Data analysis was performed using FlowJo software v10.6.2 (BD Biosciences RRID:SCR_008520).

Generation of primary human AML patient-derived xenograft (PDX) models

Primary human AML samples derived from whole peripheral blood or BM MNCs were depleted of $CD3^+$ T lymphocytes (Miltenyi Biotech), incubated with OKT1 antibody for 30 minutes on ice and transplanted via tail vein injection into 6-week-old NOD-*Prkdc*^{scid}/*Il2rg*$^{-/-}$/Tg(CMV-KITLG,CSF2,IL3) (NSG-SGM3) mice (JAX) conditioned with 200 cGy of gamma irradiation. Mice were bled monthly to assess the presence of human $CD45^+$ cells in the blood. BM aspiration was performed to assess the level of hCD45 chimerism.

In vivo administration of PARP and ATR inhibitors

For *in vivo* drug administration, olaparib (PARPi; LC Labs #9201) was dissolved in vehicle (10% DMSO and 20% cyclodextrin in sterile H_2O) and administered via intraperitoneal (i.p.) injection at 50 mg/kg per dose twice daily. For *MLL-AF9* cohorts, BM-derived primary *MLL-AF9* leukemia cells were transplanted into sub-lethally irradiated CD45.1 mice via intravenous tail vein injection. Starting from day 11 post-transplant, mice were randomly assigned to treatment groups and received treatments at a regimen of 5 days on/2 days off per cycle for a total of 3 cycles. For Kaplan-Meier survival analysis, the Mantel-

Cox log-ranked test was used to calculate median survival. For PDX experiments, bone marrow mononuclear cells from primary transplanted NSG-SGM3 mice were expanded into a larger cohort of NSG-SGM3 mice. Once engraftment was confirmed from bone marrow aspiration (hCD45% > 0.1%), mice were randomized into treatment groups and received treatments at a regimen of 5 days on/ 2 days off per cycle for a total of 6 cycles. For *in vivo* combination drug administration, olaparib (PARPi; LC Labs #9201) and AZD6738 (ATRi; AdooQ Bioscience #A15794) was dissolved in vehicle (10% DMSO and 20% cyclodextrin in sterile H_2O) and administered via intraperitoneal (i.p.) injection at 50 mg/kg per dose once daily. After the drug treatments, mice were sacrificed to obtain bone marrow (right and left femur and hip bones together). Bones were flushed in 3 mL PBS + 2% FBS and cells were centrifuged at 500 x g for 5 min. Cells were resuspended in 200 μL of PBS + 2 % FBS and counted using the Vi-CELL Blu viability analyzer (Beckman Coulter) and analyzed for human $DAPI^-$ $CD45^+$ and $CD33^+$ engraftment on a FACSCelesta or BD FACSymphony analyzer (BD Biosciences).

ARCHER and BROCA analysis

Genomic DNA was isolated from 5×10^6 viably frozen primary AML cells using DNeasy Blood and Tissue kit (Qiagen #69504). Genomic DNA was quantified using a Qubit® 2.0 Fluorometer (ThermoFisher). Sequencing libraries were prepared using the VariantPlex-HGC Core Myeloid Kit for Illumina (ArcherDx, Boulder, CO) according to the manufacturer's instructions and using 250 ng DNA input into library preparation. Finished sequencing libraries were quantified using the KAPA Library Quant Kit for Illumina (Roche Sequencing, Indianapolis, IA) and pooled in equimolar ratios. Libraries were sequenced using a P1–300 flow cell on an Illumina NextSeq 2000 or a 300-cycle v2 reagent kit on an Illumina MiSeq (Illumina, Inc., San Deigo, CA) using a using a paired-end, 151 base pair (PE151) sequencing configuration. The median raw read count obtained was 3,882,007. Resulting sequencing data were analyzed using Archer Analysis v7.2.1–1 (RRID:SCR_015854).

BROCA-GO (45–47) is a targeted next generation sequencing assay which identifies all classes of mutations in gynecologic cancer susceptibility genes, genes associated with HRR, and other genes frequently altered in gynecologic cancers. For BROCA sequencing analysis genomic DNA was isolated from 5×10^6 K562 $SRSF2^{WT}$ and $SRSF2^{P95H}$ cells to determine mutations in HRR pathway genes (Supplementary Table S6).

RNA-seq library generation

Total RNA was isolated from 5×10^6 K562 WT and K562 $SRSF2^{P95H}$ or $U2AF1^{S34F}$ cells using TRIzol according to the manufacturer's instruction. Quality of isolated RNA was determined using Agilent RNA 6000 Nano chip using the Agilent 4200 TapeStation platform. Quantification was performed using NanoDrop spectrophotometer (Thermo). Total RNA samples with RNA integrity number (RIN) > 8 were selected for Illumina sequencing library preparation. 1 μg of DNA free total RNA was used to prepare the library using Ultra II Directional RNA Library Prep Kit for Illumina (New England Biolabs #E7760L). All library preparation was conducted according to the manufacturer's instructions. Paired

end sequencing (100 bp) of the libraries were performed using an Illumina NovaSeq SP platform.

Differential Gene Expression and Splicing analysis

RNA seq reads were processed for gene expression and alternative splicing. After read quality control and adapter trimming with FastQC (https://www.bioinformatics.babraham.ac.uk/projects/fastqc/) read alignment (GRCh38, Ensemble (48)) and initial quantification was performed using Salmon1.10.2 (49). Counts where prefiltered for transcripts with a minimum count ≥ 30 followed by differential expression analysis using DESeq2 (RRID:SCR_000154) (50), comparing wildtype to mutant samples. Significant changes were determined using a cutoff of |Log2 fold change| ≥ 0.585 and p-value ≤ 0.05. Gene set enrichment analysis was performed using GSEApy v1.0.4 on a preranked list of genes sorted by their splicing factor mutant vs. wildtype log 2-fold change. GSEA was performed with 10,000 permutations and an FDR cut-off of 0.25. For splicing analysis reads were aligned (GRCh38, Ensemble) and splicing changes were quantified using RMATS-turbo 4.1.1 (51–53) with the novel splice site detection feature enabled. Significant splicing events were determined using a cutoff of |PSI|≥ 0.1 and FDR ≤ 0.05. To determine changes in splicing of homologous recombination genes, significant splicing events were filtered using KEGG pathway hsa03440 (54,55).

Data Availability

Raw sequencing files can be accessed from the SRA database, under BioProject ID numbers: PRJNA1013209 (genomics data) and PRJNA1012481 (RNA-seq data). All other raw data are available upon request from the corresponding authors.

RESULTS

Spliceosome gene mutations confer sensitivity to PARP inhibitors.

To identify novel vulnerabilities that could sensitize SF-mutant cells, we first generated an isogenic murine leukemia model by retroviral overexpression of the *MLL-AF9* fusion oncogene on a *Srsf2*$^{P95H/+}$ background (Supplementary Fig. S1A), a mutational combination that is found in ~10% of adult *MLL*-rearranged leukemias (56). Using a focused class of inhibitors targeting different DNA damage response pathways and genotoxic drugs that inhibit DNA replication or DNA metabolic processes, we performed an *in vitro* drug screen and scored cell viability relative to DMSO-treated cells (Fig. 1A; Supplementary Table S5). The area under the curve (AUC) value as a cumulative measure of compound sensitivity was calculated to assess the differential normalized AUC (ΔAUC) between *MLL-AF9* Srsf2 wildtype (Srsf2^{WT}) and *MLL-AF9* Srsf2^{P95H} cells (Fig. 1B; Supplementary Table S5). Inhibitors targeting Type-I PRMT (MS023), CDK4/6 (palbociclib and ribociclib), and ATR (VE821 and AZD6738) selectively sensitized Srsf2^{P95H} cells relative to Srsf2^{WT} cells, consistent with previous reports (13,23) (Supplementary Fig. S1B; Supplementary Table S5) and are correlated with positive ΔAUC values (Fig. 1B). Unexpectedly, Srsf2^{P95H} cells displayed increased sensitivity to different inhibitors (olaparib, veliparib, rucaparib, and talazoparib) targeting ADP-ribosyltransferases (PARP) 1/2 enzymes (Figs. 1C–D, Supplementary Figs. S1C–E). Olaparib (PARPi) significantly reduced cell proliferation in

Srsf2^{P95H} cells more than PARPi-treated Srsf2^{WT} cells (Fig. 1E). Consequently, PARPi induced higher apoptosis in Srsf2^{P95H} cells than Srsf2^{WT} cells without significantly affecting cell cycle progression (Fig. 1F; Supplementary Fig. S1F). Srsf2^{P95H} cells are also sensitive to the PARP1-specific inhibitor, AZD5305 (Fig. 1G), suggesting that the sensitivity is caused by inhibiting PARP1 enzyme. This is further confirmed by *Parp1* deletion in Srsf2^{P95H} cells (Srsf2^{P95H} + sg.Parp1), which significantly reduced cell proliferation compared to Srsf2^{P95H} cells transfected with a gRNA targeting Rosa26 locus (Srsf2^{P95H} + sg.Rosa26, Fig. 1H). Taken together, these results identified PARP1 as a novel dependency in Srsf2-mutant leukemias.

To examine whether the observed PARPi sensitivity is conserved in human leukemias expressing *SRSF2* gene mutations, we used a pair of previous established isogenic human K562 cells expressing *SRSF2^{WT}* or the *SRSF2^{P95H}* mutation from the endogenous locus (57). SRSF2^{P95H} cells showed increased sensitivity to olaparib and rucaparib (Fig. 1I, Supplementary Fig. S1G). Finally, PARPi treatment or genetic deletion of *PARP1* in SRSF2^{P95H} cells reduced cell proliferation and caused increased cell death in SRSF2^{P95H} cells compared with SRSF2^{WT} cells (Figs. 1J–K, Supplementary Fig. S1H).

Next, we determined the sensitivity to PARPi in leukemias based on their SF-mutational status *in vivo*. Established Srsf2^{WT} or Srsf2^{P95H} leukemias were transplanted into syngeneic recipient mice (Supplementary Fig. S1I). Eleven days post-transplant, recipient mice were randomly assigned to receive either vehicle or PARPi for a total of 15 doses. Recipient mice transplanted with Srsf2^{WT} leukemias showed no differential survival benefit when treated with either vehicle or PARPi (Fig. 1L). In contrast, PARPi treatment significantly prolonged the survival of recipient mice transplanted with Srsf2^{P95H} leukemias compared to vehicle-treated mice. Taken together, these results demonstrate that Srsf2^{P95H} murine leukemias are more sensitive to PARP inhibition *in vivo*.

The observed PARPi sensitivity in SRSF2-mutant leukemias led us to ask whether PARPi sensitivity extends to mutations affecting other SF genes. To address this question, we generated an additional pair of isogenic leukemia on an *U2af1$^{S34F/+}$* background (Supplementary Fig. S1A). *MLL-AF9 U2af1$^{S34F/+}$* (U2af1^{S34F}) leukemia cells were more sensitive to ATRi compared to *MLL-AF9 U2af1$^{+/+}$* (U2af1^{WT}) cells, as previously described (Supplementary Fig. S2A) (13). U2af1^{S34F} cells also exhibited increased sensitivity to different PARP inhibitors measured by positive ΔAUC and lower IC50 values relative to U2af1^{WT} cells (Figs. 2A–C, Supplementary Fig. S2B, Supplementary Table S5). PARPi induced higher apoptosis in U2af1^{S34F} cells than in U2af1^{WT} cells (Fig. 2D) as well as decreased cell proliferation (Fig. 2E). Moreover, K562 U2AF1^{S34F} cells also showed decreased cell proliferation upon PARPi treatment compared to their isogenic wildtype (Fig. 2F). Similar to SRSF2- and U2AF1-mutant cells, SF3B1^{K700E} K562 cells were also more sensitive to olaparib and rucaparib relative to SF3B1^{WT} cells (Supplementary Figs. 2C–D). PARPi treatment induced higher cell death in SF3B1^{K700E} compared to SF3B1^{WT} cells (Supplementary Fig. S2E). Additionally, PARPi also sensitized human induced pluripotent stem cell (iPSC)-derived hematopoietic progenitors expressing either *SRSF2^{P95L}*, *U2AF1^{S34F}* or *SF3B1^{G742D}* mutations relative to their isogenic control cells (Supplementary Figs. S2F–H). Finally, we tested PARP inhibitor sensitivity across a panel

of human AML cell lines. AML cells that harbor spliceosome mutations (K052, *SRSF2*^{P95H}; NKM1, *U2AF1*^{S34F}; HNT34, *SF3B1*^{K700E}) were more sensitive to three different PARP inhibitors compared to AML cells without known spliceosome mutations (Figs. 2G–H; Supplementary Figs. S2I). Taken together, these findings demonstrate that PARP1 is a novel dependency in leukemias that carry spliceosome gene mutations.

SRSF2^{P95H} and U2AF1^{S34F} cells trigger PARP1 response and prevent accumulation of DNA damage.

The observed PARPi sensitivity suggests that SF-mutant leukemias depend on PARP activity for survival. To monitor PARP activity in SF-mutant cells, we examined Mono- and Poly-ADP-ribosylated chain (MAR/PAR) levels in whole cell extracts as a measurement of total cellular PARP activity. MAR/PAR levels were readily detected in cells using two different antibodies, MAR/PAR and pan-ADPr (Figs. 3A–B; Supplementary Figs. S3A–B). SRSF2^{P95H} and U2AF1^{S34F} cells displayed higher MAR/PAR levels compared to their respective wildtype cells. Acute PARPi treatment completely abrogated MAR/PAR levels in SRSF2^{P95H} and U2AF1^{S34F} cells. Moreover, *PARP1* deletion by CRISPR-Cas9 abrogated the elevated MAR/PAR levels in SRSF2^{P95H} and U2AF1^{S34F} cells, indicating that the increased level of MAR/PAR in SF-mutant cells is primarily driven by PARP1 (Figs. 3C–D). To determine the consequence of PARPi exposure in SF-mutant cells, we treated SRSF2^{P95H}, U2AF1^{S34F}, and their respective isogenic wildtype cells with PARPi for 24–48 hours and measured γH2AX levels as a marker of DNA damage. In untreated cells, there was no significant difference in γH2AX levels between SRSF2^{WT} and SRSF2^{P95H} cells (Figs. 3E–F). Upon PARPi treatment, both SRSF2^{WT} and SRSF2^{P95H} cells showed higher γH2AX levels. Importantly, PARPi-treated SRSF2^{P95H} cells exhibited higher γH2AX levels than PARPi-treated SRSF2^{WT} cells. Similarly, PARPi-treated U2AF1^{S34F} cells also displayed higher γH2AX levels than PARPi-treated U2AF1^{WT} cells (Supplementary Fig. S3C). These results suggest that PARP1 plays a critical role in preventing the accumulation of DNA damage in SF-mutant cells.

We next sought to investigate which cell cycle phase accumulates DNA damage after PARPi treatment. First, to follow the cell cycle status in individual cells in asynchronous cell populations, we pulse-labeled newly synthesized DNA with EdU, a modified thymidine nucleoside incorporated into the DNA of actively proliferating cells. Cells undergoing DNA replication displayed high levels of EdU intensity after pulse-labeling (Supplementary Fig. S3D). We established a cell cycle profile using quantitative image-based cytometry (QBIC), comparing EdU and DAPI in individual populations to identify G1, S, and G2 cell populations. We then evaluated DNA damage levels, marked by γH2AX in different cell cycle populations. PARPi treatment caused drastic increases in γH2AX levels in SRSF2^{P95H} cells compared to SRSF2^{WT} cells in S and G2, and to a lesser extent in G1, phases of the cell cycle (Supplementary Fig. S3E), suggesting that the majority of the observed DNA damage may arise during DNA replication. Taken together, these data suggest that SF-mutant leukemias elicit a PARP1 response to prevent accumulation of DNA damage as cells undergo DNA replication.

PARPi sensitivity in SF-mutant leukemias is not due to HR defect.

PARP inhibitors preferentially kill cells with defective homologous recombination (HR)-mediated DNA repair (58), which prompted us to investigate whether SF-mutant cells are HR defective. We first asked whether HR-related genes were differentially regulated in SF-mutant leukemias. RNA-seq analysis revealed a limited number of differentially expressed or differentially spliced genes in the HR pathway between $SRSF2^{WT}$ and $SRSF2^{P95H}$ cells (Supplementary Tables S7–8; Supplementary Fig. S3F). Similarly, there were no major differences in either gene expression or alternative splicing of HR-related genes in $U2AF1^{S34F}$ cells compared to $U2AF1^{WT}$ cells (Supplementary Tables S9–10; Supplementary Fig. S3G). No significant enrichment in HR gene sets by GSEA were found in $SRSF2^{P95H}$ and $U2AF1^{S34F}$ cells compared to their respective wildtype cells (Supplementary Table S11). Furthermore, protein levels of several known HR regulators were also similar between $SRSF2^{WT}$ and $SRSF2^{P95H}$ cells (Supplementary Fig. S3H). Lastly, we performed targeted gene capture followed by sequencing in K562 $SRSF2^{WT}$ and K562 $SRSF2^{P95H}$ cells using the BROCA assay, which detects a panel of HR and DNA damage repairs genes (45). While we found mutations in *TP53* and *ERCC6*, along with *CDKN2A* deletion (Supplementary Table S6), which is consistent with the mutational status of K562 cells, our analysis did not identify somatic mutations in other HR-related genes.

Next, we examined the level of chromatin bound Rad51, a marker of HR, after PARPi treatment. PARPi increased chromatin-bound Rad51 in γH2AX-positive $SRSF2^{WT}$ compared to DMSO-treated $SRSF2^{WT}$ cells (Supplementary Figs. S3I–J). BRCA1 is a key regulator of RAD51 loading in HR in S phase (59). To test whether BRCA1-depletion would result in a decrease in chromatin-bound Rad51, we assessed Rad51 loading after olaparib treatment in S phase cells. We pulsed cells with EdU to mark S phase cell population for immunofluorescence analysis. Indeed, BRCA1-depletion by shRNA significantly reduced chromatin-bound Rad51 in EdU/γH2AX-double positive $SRSF2^{WT}$ cells treated with PARPi (Supplementary Fig. S3K; Figs. 3G–H). Interestingly, $SRSF2^{P95H}$ cells also showed robust chromatin bound Rad51 after PARPi treatment. BRCA1 depletion also reduced Rad51 loading similar to $SRSF2^{P95H}$ shBRCA1-depleted cells, suggesting that the BRCA1-mediated HR pathway is intact in $SRSF2^{P95H}$ cells. In agreement with this notion, whereas BRCA1 depletion did not affect $SRSF2^{WT}$ and $SRSF2^{P95H}$ cell viability (Supplementary Fig. S3L), BRCA1 depletion reduced viability of both $SRSF2^{WT}$ and $SRSF2^{P95H}$ cells to the same extent following PARPi treatment (Fig. 3I), suggesting that $SRSF2^{P95H}$ cells have intact BRCA1-regulated HR.

Next, we directly measured HR activity in $SRSF2^{P95H}$ mutant cells by the CRISPR-Cas9/mClover assay (60). The assay measures the HR-dependent insertion of a *mClover*-containing “donor” cassette sequence into Cas9-generated double-stranded breaks in the *LMNA* gene, which results in the expression of a green, fluorescent Lamin A/C protein that can be monitored by flow cytometry (Supplementary Fig. S3M). Using the CRISPR-Cas9/mClover assay, we first treated K562 cells with the ATR inhibitor, VE-821 and confirmed that ATR was required for efficient HR as previously reported (59) (Supplementary Fig. S3N). We also confirmed that $SF3B1^{K700E}$ cells have reduced HR function compared to $SF3B1^{WT}$ cells, which is consistent with a recent report (Supplementary Fig. S3O) (61).

In contrast, there were no significant differences in the HR efficiency in SRSF2^{P95H} cells compared to SRSF2^{WT} cells (Fig. 3J), suggesting that SRSF2^{P95H} cells are HR-proficient. SRSF2^{P95H} cells also promote HR repair efficiently using the well-established DR-GFP reporter assay (Supplementary Fig. S3P) (43). U2AF1^{S34F} cells are also proficient in promoting HR repair (Fig. 3K). Taken together, these results provide robust evidence that the PARPi sensitivity observed in SRSF2^{P95H} and U2AF1^{S34F} cells is not due to defective HR repair capacity. Finally, although loss of CINP was implicated in PARPi sensitivity in SF3B1-mutant melanoma cells (62), we did not observe any change in CINP protein levels in either SRSF2^{P95H} or U2AF1^{S34F} cells compared to wildtype cells (Supplementary Fig. S3P). These observations raise the intriguing question as to what the underlying cause is for the increased PARPi sensitivity in SF-mutant leukemias.

SF-mutant leukemias uniquely elicit a PARP1 response at R loops.

We next determined how SF-mutant leukemias elicit a PARP1 response. Recently, biochemical studies demonstrated that PARP1 can directly associate with R-loop structures *in vitro* (41), suggesting a potential role for PARP1 in regulating R-loop homeostasis. This led us to hypothesize that the observed PARPi sensitivity in SF-mutant cells is due to altered PARP1 activity at R loops. To answer this, we developed proximity ligation-based strategies to quantify the level of PARP1 activity at R loops in SF-mutant cells. We first confirmed that SRSF2^{P95H} cells have higher levels of R loops compared to SRSF2^{WT} cells, measured by immunostaining using anti-S9.6, an antibody that has affinity for RNA:DNA hybrids (Supplementary Fig. S4A). To confirm that PARP1 physically associates with R loops, we enriched R loops using anti-S9.6 antibody and performed western blot for PARP1. Indeed, S9.6 pulled down PARP1 in K562 parental cell extracts but not in K562 PARP1^{KO} cells (Supplementary Fig. S4B). To measure PARP1 association to R loops in SRSF2^{P95H} cells, we performed proximity ligation assay (PLA) using antibodies to PARP1 and R loops (PARP1:S9.6). Indeed, we detected robust PLA foci when both antibodies were applied (Figs. 4A–B), confirming that PARP1 can indeed associate with R loops at steady state. SRSF2^{P95H} cells exhibited a significantly increased number of PARP1:S9.6 PLA foci per nucleus relative to SRSF2^{WT} cells. Moreover, the number of PARP1:S9.6 PLA foci were reduced in SRSF2^{P95H} PARP1^{KO} cells, suggesting that the observed PLA foci is PARP1-dependent.

To monitor PARP1 ADP-ribosylation activity at R loops, we developed a novel PLA using antibodies specific to ADP-ribosylated chains and R loops (MAR/PAR:S9.6 PLA). For optimization, we induced R loops by treating cells with Pladienolide-B (Plad-B), a splicing modulator that targets SF3B1, the core component of the U2 small nuclear ribonucleoprotein (U2 snRNP) complex (12,13,63–65). We treated cells with Plad-B at nanomolar concentration for 6 hours and assessed R-loop levels by S9.6 immunostaining. Consistent with previous findings, we observed an increase in S9.6 foci after Plad-B treatment (Supplementary Figs. S4C–D). RNase H1 overexpression, an enzyme to specifically resolves R loops, reduced Plad-B-induced S9.6 foci, validating that Plad-B indeed triggered R-loop accumulation. At 6-hour time point, we did not observe any increased DNA damage, measured by γH2AX, until 24h after Plad-B treatment (Supplementary Figs. S4E–F). In addition, we also detected robust MAR/PAR levels after

as early as 2 hours after Plad-B treatment compared to DMSO control (Supplementary Fig. S4G). Deletion of the *PARP1* gene by CRISPR-Cas9 attenuated the induced MAR/PAR levels (Supplementary Fig. S4H). Moreover, RNase H1 overexpression in Plad-B-treated cells suppressed MAR/PAR levels, suggesting that Plad-B-induced PARP1 response arises from R loops (Supplementary Fig. S4I). We used a 6-hour Plad-B treatment timepoint to assess PARP1 activity at R loops without inducing DNA damage for PLA assay. Indeed, Plad-B-treated cells had increased MAR/PAR:S9.6 PLA foci compared to DMSO-treated cells only when both antibodies, but not in no antibody or S9.6 antibody alone, were used (Supplementary Figs. S4J–K). Further, PARPi treatment reduced MAR/PAR:S9.6 PLA foci, suggesting that the PLA foci is PARP1-dependent. Taken together, our cumulative data suggests that Plad-B induced R-loop accumulation and elicits a PARP1 response at R loops without any observable induced DNA damage.

Having successfully established MAR/PAR:S9.6 PLA, we next assess PARP1 activity at R loops in SF-mutant cells. Consistent with the increased PARP1:S9.6 PLA foci, $SRSF2^{P95H}$ cells also exhibited a significantly higher number of MAR/PAR:S9.6 PLA foci compared to $SRSF2^{WT}$ cells (Figs. 4C–D). MAR/PAR:S9.6 PLA foci were detected in $SRSF2^{P95H}$ cells when both, but not individual antibodies, were applied (Supplementary Fig. 4L). Olaparib is known to inhibit PARP1 activity and to trap PARP1 on chromatin. Consistent with this notion, PARPi treatment significantly reduced the number of MAR/PAR:S9.6 PLA foci (Figs. 4C–D) while causing an increase in PARP1:S9.6 PLA foci in $SRSF2^{P95H}$ cells, suggesting that olaparib inhibits PARP1 activity while retaining PARP1 association to R loops (Supplementary Fig. 4M). The addition of purified *e. coli* RnaseH (eRH) prior to PLA assay significantly reduced the number of MAR/PAR:S9.6 PLA foci, validating that the MAR/PAR:S9.6 association is an R-loop-specific phenomenon (Figs. 4C–D). Finally, we assessed whether PARP1 is active at R loops in established splicing-mutant AML cell lines K052 and NKM1 cells, which harbor endogenous $SRSF2^{P95H}$ or $U2AF1^{S34F}$ mutations, respectively. First, we assessed R-loop levels in SF-mutant leukemias. Consistent with our observation in isogenic K562 $SRSF2^{WT}$ and $SRSF2^{P95H}$ cells, both K052 and NKM1 cells exhibited higher R-loop levels relative to OCI-AML3 cells, a leukemia cell line that does not carry any splicing factor mutations (Supplementary Figs. S4N–O). Importantly, the number of MAR/PAR:S9.6 PLA foci in K052 and NKM1 cells were significantly higher than OCI-AML3 cells (Fig. 4E–F). Taken together, these results demonstrate that PARP1 associates with and mediates ADP-ribosylation activity at R loops in SF-mutant leukemias.

PARP inhibition selectively sensitizes SF-mutant leukemias caused by R-loop accumulation.

Given that PARP1 exerts enzymatic activity at R loops and that PARPi-induced DNA damage leads to cell death in SF-mutant leukemias, we asked whether the observed PARPi sensitivity in SF-mutant leukemias can be attributed to R-loop accumulation. To address this question, we generated $SRSF2^{WT}$ and $SRSF2^{P95H}$ cells that express a doxycycline-inducible, GFP-tagged nuclear RNase H1, an enzyme specifically hydrolyzes the RNA moiety within RNA:DNA hybrids to remove R-loop structures (12,66). Induction of RNase H1 expression in $SRSF2^{P95H}$ cells reduced MAR/PAR levels, showing that SF-mutant-induced ADP-ribosylation is R-loop-dependent (Fig. 4G). We next asked whether

PARPi-induced DNA damage is caused by R loops in SRSF2^{P95H} cells. We treated SRSF2^{P95H} cells with PARPi in the presence or absence of RNase H1 expression. PARPi-treated SRSF2^{P95H} cells exhibited higher γH2AX levels than PARPi-treated SRSF2^{WT} cells (Supplementary Fig. S4P). Moreover, RNase H1 overexpression in PARPi-treated SRSF2^{P95H} cells reduced γH2AX levels to a similar level as PARPi-treated SRSF2^{WT} cells, suggesting that the PARPi-induced DNA damage in SRSF2^{P95H} cells arises from R-loops. RNase H1 expression also rescued PARPi-induced cell growth inhibition in SRSF2^{P95H} cells (Fig. 4H). The suppression of MAR/PAR, PARPi-induced DNA damage and cell growth inhibition in SRSF2^{P95H} cells prompted us to ask whether aberrant R loops also contribute to PARPi sensitivity in U2AF1^{S34F} cells. Similar to SRSF2^{P95H} cells, RNase H1 expression also reduced basal MAR/PAR levels, reduced PARPi-induced DNA damage, and importantly, rescued PARPi-induced cell growth inhibition in U2AF1^{S34F} cells (Figs. 4I–J; Supplementary Fig. S4Q). Finally, PARPi-induced apoptosis in SRSF2^{P95H} cells was suppressed by RNase H1^{WT} expression, but not by the catalytically inactive RNase H1^{D210N} mutant construct (Fig. 4K). Taken together, these results demonstrate that PARP1 activity is critical to prevent R-loop-associated genomic instability in SF-mutant leukemias.

PARPi induce R-loop-associated ATR response caused by increased transcription-replication collisions in SF-mutant leukemias.

We observed that PARPi treatment induced higher R-loop levels in SRSF2^{P95H} cells compared to DMSO-treated SRSF2^{P95H} cells (Figs. 5A–B). Since accumulated R loops may collide with DNA replication during S phase, we asked whether PARPi-induced R loops in SRSF2^{P95H} cells cause more transcription-replication collisions (TRC). To measure the collision between transcription and replication machineries in SRSF2^{P95H} cells, we performed PLA using antibodies that detect the elongating form of RNA polymerase II (Pol2-pS2) and PCNA, respectively (Supplementary Fig. S5A). TRC PLA foci were detected in SRSF2^{P95H} cells only when both antibodies were used (Supplementary Fig. S5B). At basal level, the numbers of TRC PLA foci were higher in SRSF2^{P95H} cells than in SRSF2^{WT} cells (Figs. 5C–D, Supplementary Figs. S5C–D). PARPi further increased TRC PLA foci numbers in SRSF2^{P95H} cells. Importantly, overexpression of RNase H1 in SRSF2^{P95H} cells significantly reduced PARPi-induced TRC PLA foci, suggesting that PARPi-induced TRC arises from R loops. Taken together, these results demonstrate that PARP1 prevents transcription-replication collisions in SRSF2^{P95H} mutant cells.

The collision between RNA polymerase II and replication forks is a potential source of replicative stress in cells that could activate ATR signaling (42,67). This prompted us to investigate whether PARPi-induced TRC in SRSF2^{P95H} cells triggers an ATR response. We treated SRSF2^{WT} and SRSF2^{P95H} cells with PARPi for 24 hours and monitored phosphorylated RPA at Ser33 (RPA32 pS33), an ATR substrate and a surrogate for ATR kinase activity (13). At baseline, RPA32 pS33 levels were higher in SRSF2^{P95H} cells compared to SRSF2^{WT} cells (Fig. 5E). We also observed higher phosphorylation of Chk1, another ATR substrate, but not Chk2, in SRSF2^{P95H} cells compared to SRSF2^{WT} cells (Supplementary Fig. S5E). PARPi further enhanced RPA32 pS33 levels in SRSF2^{P95H} cells compared to SRSF2^{WT} cells (Fig. 5E). This effect was abrogated in the presence of ATRi, suggesting that ATR activity was enhanced in PARPi-treated SRSF2^{P95H} cells (Fig.

5E). Importantly, RNase H1 overexpression in PARPi-treated SRSF2^{P95H} cells reduced RPA32 pS33 levels, suggesting that the increased ATR response is R-loop-dependent (Supplementary Fig. S5F). These results suggest that PARPi treatment induced R-loop accumulation, causing more TRC, thereby eliciting an elevated ATR response in SF-mutant cells.

ATR inhibition potentiates PARPi sensitivity in SF-mutant cells.

The increased ATR response in SF-mutant cells upon PARPi treatment prompted us to ask whether ATRi can exacerbate PARPi sensitivity in SF-mutant cells. The combination of PARPi and ATRi (PARPi+ATRi) induced higher γH2AX levels in SRSF2^{P95H} cells compared to SRSF2^{WT} cells (Fig. 5F). In contrast, ATRi, but not ATM inhibitor (ATMi, KU-55933) induced γH2AX in PARPi-treated SRSF2^{P95H} cells. The γH2AX levels in SRSF2^{P95H} cells treated with PARPi+ATRi were also higher than cells treated with either PARPi or ATRi alone (Supplementary Fig. S5G). Importantly, expression of RNase H1 in PARPi+ATRi-treated SRSF2^{P95H} cells reduced γH2AX levels, showing that the DNA damage induced by PARPi+ATRi in SRSF2^{P95H} cells arises from R loops (Fig. 5G). Consistent with the increase in γH2AX levels, PARPi combined with ATRi, but not ATMi, further increased cell growth inhibition in SRSF2^{P95H} cells compared to SRSF2^{WT} cells (Supplementary Fig. S5H; Figs. 5H–I).

To determine whether the observed synergistic effect of PARPi+ATRi in SRSF2^{P95H} cells can be extended to other spliceosome mutations, we evaluated PARPi+ATRi sensitivity in U2AF1^{S34F} mutant cells. First, PARPi+ATRi treatment in U2AF1^{S34F} cells induced higher γH2AX levels compared to PARPi+ATRi-treated U2AF1^{WT} cells, which can be suppressed by RNase H1 expression (Supplementary Fig. S5I), suggesting that the increased DNA damage, in part, arises from R loops. PARPi+ATRi combination also reduced cell growth and induced higher cell death in U2AF1^{S34F} cells compared to treatment with PARPi+ATRi-treated U2AF1^{WT} cells (Supplementary Fig. S5J). Finally, the PARPi and ATRi combination also synergistically reduced cell viability in murine Srsf2^{P95H} and U2af1^{S34F} murine leukemia cells compared to their respective SF-wildtype leukemic cells (Figs. 5J–L). Taken together, these results demonstrate that PARPi further induces R-loop accumulation in SF-mutant leukemias, leading to increased TRC, rendering cells more dependent on ATR signaling for survival.

Combined PARPi and ATRi synergize in killing primary human SF-mutant AML cells.

SF-mutant leukemias are hyper-sensitive to the combined PARPi and ATRi treatment. This led us to determine whether this observation can be extended to primary AML patient samples. We first tested PARPi and ATRi sensitivities across a panel of 17 primary AML patient samples, 7 of which were wildtype for spliceosome mutations, and 10 contained either *SRSF2* (n= 5) or *U2AF1* (n=5) hotspot mutations (Supplementary Fig. S6A; Supplementary Table S4). SF-mutant AML cells showed elevated sensitivity to PARPi or ATRi relative to SF-wildtype AMLs *ex vivo* (Figs. 6A–B). Further, the combination of PARPi and ATRi resulted in synergistic killing of SF-mutant AML cells compared to SF-wildtype mutant AML cells (Fig. 6C; Supplementary Fig. S6B). Finally, to confirm the observed synergy in an *in vivo* pre-clinical model, we generated primary

AML patient derived xenografts (PDX) from three AML patients; two of the patients harbored either a *U2AF1* or *SRSF2* mutation, and the third patient lacked mutations in spliceosome-related genes. Once successful engraftment of human AMLs was detected from bone marrow aspirates (defined as >0.1% human CD45+ cells), mice were randomized to receive either vehicle or combined treatment of PARPi (50 mg/kg/day) and ATRi (50 mg/kg/day) (Supplementary Fig. S6A). Mice received six treatment cycles, where each cycle encompassed five days of treatment followed by two days of rest. We first tested whether this combination treatment regimen could be tolerated in C57BL/6 mice. Apart from a mild reduction in BM cellularity and minor changes to the immune cell composition in the spleen, this combination treatment regimen did not cause any bodyweight loss or overt hematologic toxicities based on peripheral blood profiles, or any observable gastrointestinal and ocular toxicities (Supplementary Fig. S7A–I). After six cycles of PARPi+ATRi treatment in PDX models, both *U2AF1*-mutant and *SRSF2*-mutant PDXs show significant reductions in leukemia burden, which was determined by the percentages of hCD45+ and hCD33+ cells in the bone marrow (Figs. 6D–E). On the other hand, the same treatment regimen did not reduce the disease burden in the splicing factor-wildtype PDX compared to vehicle-treated group (Figs. 6D–E). Interestingly, the average spleen size of PARPi+ATRi-treated SF-wildtype PDX mice were significantly larger than vehicle-treated mice, suggesting increased disease burden (Supplementary Fig. S8A). In contrast, there were no observable changes in spleen weight of *SRSF2*-mutant or *U2AF1*-mutant PDXs following combination treatment (Supplementary Figs. S8A). Additional analysis showed that the combination treatment regimen did not cause any major changes in the blood profiles and BM cellularity in PDX models compared to their vehicle-treated counterparts (Supplementary Figs. S8B–E). Taken together, our *ex vivo* and *in vivo* data demonstrate that combination treatment with PARP and ATR inhibitors is specifically effective against splicing factor-mutant leukemias, irrespective of the presence of other existing co-mutations.

PARP activity at R loops and transcription-replication collisions are potential predictive biomarkers for PARPi and ATRi sensitivities in human SF-mutant leukemias.

The increased PARP1 activity at R loops and R-loop-associated TRC in SF-mutant cells highlight potential indicators of R-loop response and predictor of PARPi and ATRi sensitivity. To test this possibility, we first assessed PARP1 activity at R-loops by MAR/PAR:S9.6 PLA using primary patient AML cells (Figs. 6F–G). MAR/PAR:S9.6 PLA foci were readily detected in all four SF-mutant AML samples (Fig. 6F). Importantly, numbers of PLA foci were significantly higher in SF-mutant AML compared to SF-wildtype AML, suggesting that PARP1 response is elevated at R loops in SF-mutant AML cells (Fig. 6G). We next monitored TRC using Pol2-pS2:PCNA PLA and also observed an increase in TRC foci numbers in SF-mutant leukemias (Figs. 6H–I). Taken together, primary human AML harboring SF mutations exhibited increased R-loop-associated PARP1 activity and TRC, highlighting the potential predictive biomarkers for PARPi and ATRi sensitivities.

DISCUSSION

There is growing evidence that RNA splicing perturbation by spliceosome gene mutations promotes R-loop accumulation and genomic instability if the hybrid structures are not

properly resolved. In this study, we present compelling evidence that PARP1 associates with and initiates ADP-ribosylation at R loops in SRSF2- and U2AF1-mutant cells (Fig. 7). We also identify that PARP1 response at R loops suppresses transcription-replication conflict to prevent further genomic instability in SF-mutant cells. We reason that the unique PARP1 dependency forms the basis of the enhanced PARP inhibitor sensitivity in SRSF2- and U2AF1-mutant leukemias. We further show that the observed PARPi sensitivity in SRSF2- and U2AF1-mutant cells is independent of defective homologous-recombination (HR) that are commonly associated with increased PARPi response in BRCA1/2-mutant cancers. Importantly, we developed an assay that allows for direct monitoring of PARP1 activity at R loops, which can be used as an indicator of R-loop-induced PARP1 response and a predictive biomarker for PARPi sensitivity in primary AML patients. In principle, findings from this study have implications for expanding the use of PARP inhibitors to cancers that exhibit inherent defects in RNA splicing and R-loop homeostasis.

PARP1 is an abundant nuclear protein that post-translationally attaches ADP-ribosylated chains to itself and to multiple proteins during DNA repair, stabilizes replication forks, modifies chromatin structures, and regulates transcription (58,68–70). Emerging proteomic and biochemical analyses have also shown that PARP1 can physically associate with R-loops, suggesting a role in R-loop regulation (41,68,71–73). Our data suggest that in the presence of spliceosome gene mutations, cells become hyper-reliant on PARP1 to suppress excess DNA damage arising from elevated R loops as well as transcription-replication collisions. Exactly how PARP1 is activated to prevent and/or resolve R loops remains to be elucidated. The most straightforward possibility is that PARP1 ADP-ribosylates specific substrates to resolve R loops and prevent R-loop-associated DNA damage (Fig. 7). Indeed, proteomic analyses enriching ADP-ribosylated substrates identified many factors that have been implicated in R loop regulation (74). Moreover, it will also be important to determine specific R-loop loci where PARP1 functions to suppress genomic instability. Future studies will be necessary to pinpoint the exact molecular functions of these factors in the context of SF-mutant cell.

In addition to PARPi as a single therapeutic agent, we provide additional rationale for combining PARPi with ATRi to further synergize killing of SF-mutant cells. We demonstrate that PARP1 inhibition causes R loop accumulation and increased transcription-replication collisions during S phase, thereby activating ATR signaling. Importantly, R-loop suppression by RNase H1 overexpression abrogated PARPi-induced transcription-replication collisions, suggesting an R-loop-dependent mechanism. Consequently, the combination of PARPi and ATRi induced further DNA damage, causing increased cell apoptosis compared to individual agents. In the absence of ATR, R loops may lead to collapse of replication forks or are aberrantly processed by nucleases (42,75). These events could give rise to DNA double-stranded breaks, driving cells to apoptosis. Therefore, when PARP1 is inactivated in SF-mutant cells, ATR inhibition ablates this important protective mechanism at R loops, resulting in R-loops-induced DNA damage and cell death. Finally, our established PLA assay to monitor TRC could potentially be an additional biomarker that predicts ATRi sensitivity in SF-mutant leukemias warrants further evaluation. Future studies will be important to delineate the molecular basis of R-loop accumulation, PARP1 response, and R-loop-associated PARPi sensitivity in other SF-mutant myeloid malignancies. Moreover,

the recent development of PARP1-specific inhibitors such as AZD5305, which has low hematologic toxicity profiles, may be another promising therapeutic agent, particularly for relapsed/refractory MDS and secondary AML patients harboring SF mutations.

The successful use of PARP inhibitors as a frontline therapy for *BRCA1/2*-deficient cancer patients highlights the importance of synthetic lethality, a concept that can be extended to biomarker development to predict treatment responses (58). While FDA-approved PARP inhibitors are currently only used to treat solid tumor patients, there is growing interest in using PARPi in hematologic malignancies despite the rarity of *BRCA1/2* mutations. Several recent studies have provided evidence that leukemia-associated mutations in *IDH1/2*, *TET2*, *SF3B1*, and *STAG2* confer sensitivity to PARP inhibitors due to increased replication stress, replication fork stalling and impaired DNA repair capacity, consistent with known mechanisms of PARPi sensitivity (44,61,62,76–78). We provide evidence that the enhanced PARPi sensitivity in SRSF2- and U2AF1-mutant leukemia cells is driven primarily through the constant engagement of PARP1 activity at R loops to suppress TRC and DNA damage to maintain cell survival. If aberrant PARP1 activity at R loops is a unifying cellular response, PARP inhibitors may have therapeutic benefits in a broader spectrum of cancers beyond those with defective HR status. Furthermore, combination of PARPi and ATRi may provide an effective strategy to therapeutically target R-loop-associated vulnerabilities in other hematologic malignancies. In summary, our study establishes a pre-clinical rationale to test PARP inhibitors in spliceosome mutant leukemias, highlighting the potential of identifying R-loop response signatures as biomarkers for diagnostic and therapeutic monitoring purposes in human cancers. Furthermore, our study also highlights the potential of targeting different R-loop response pathways caused by spliceosome gene mutations as a new modality in cancer therapeutic strategies.

Supplementary Material

Refer to Web version on PubMed Central for supplementary material.

Acknowledgments

We thank Dr. Fouquerel for reagents, Dr. Omar Abdel-Wahab for the K562 SRSF2^{P95H} and K562 SF3B1^{K700E} cells, Dr. Jerry Radich for HL60 and THP-1 cells, members of the Nguyen and Lee laboratories for helpful discussions. M.S. is supported by AIRC Postdoctoral Fellowship (Project #28390). V. Corral is partially supported by the UMN Clinical and Translation Science Institute A-PREP program. S. Doulatov is supported by grants from the National Heart, Lung, and Blood Institute (R01 HL151651 and R01 HL169156), Kuni Foundation, and Edward P. Evans Foundation. S. Doulatov is a Scholar of the Leukemia and Lymphoma Society (1391–24). T. Skorski is supported by grants from the National Cancer Institute (R01 CA244044 and R01 CA247707) and Leukemia and Lymphoma Society Translational Research Program grant (6628–21). E.P. Papapetrou is supported by grants from the National Cancer Institute (R01 CA271418, R01 CA271331 and R01 CA260711), an Edward P. Evans Foundation Discovery Research Grant, Leukemia and Lymphoma Society Blood Cancer Discoveries Grant and a 2021 AACR-MPM Oncology Charitable Foundation Transformative Cancer Research Grant, Grant Number 21-20-45-PAPA. Z. Sachs was supported by the Lois and Richard King Assistant Professorship in Medicine at the University of Minnesota, the Clinical and Translational Science Institute at the University of Minnesota KL2 Career Development Award and K to R01 Award (NIH/NCATS ULI RR033183 & KL2 RR0333182), the Mugee Research Award for Pediatric Cancer, the Randy Shaver Cancer Research and Community Fund Award, The division of Hematology, Oncology, and Transplantation, Department of Medicine, the Masonic Cancer Center, and the University of Minnesota Foundation donors. T.A. Graubert is supported by the Leukemia and Lymphoma Society Specialized Center of Research Program 7024–21, and P50CA171963. M.J. Walter is supported by grants from the Leukemia and Lymphoma Society Specialized Center of Research Program (7024–21), National Cancer Institute (P50CA171963), and the Edward P. Evans Foundation. S.C. Lee is supported by grants from the Edward P. Evans Foundation, American Society of Hematology, Vera and Joseph Dresner Foundation, National Cancer Institute (R00

CA218896) and the Mark Foundation For Cancer Research. H.D. Nguyen is supported by grants from the Edward P. Evans Foundation, American Society of Hematology, the National Institutes of Health's National Center for Advancing Translational Sciences, grants (KL2TR002492 and UL1TR002494), and the National Heart, Lung, and Blood Institute (R01 HL163011) and the 2022 AACR Career Development Award to Further Diversity, Equity, and Inclusion in Cancer Research, which is supported by Merck, Grant Number 22-20-68-NGUY. This research is also supported by the Fred Hutchinson Cancer Center Shared Resources through NCI Cancer Center Support grants (P30 CA015704 and S10 OD028685). The authors would also like to acknowledge that the primary human AML specimens were obtained from Protocol 1690, the Fred Hutch Cancer Center/University of Washington Hematopoietic Diseases Repository (FHCC/UW-HDR).

REFERENCES

1. Anczukow O, Krainer AR. Splicing-factor alterations in cancers. RNA. 2016;22:1285–301. [PubMed: 27530828]
2. Dvinge H, Kim E, Abdel-Wahab O, Bradley RK. RNA splicing factors as oncoproteins and tumour suppressors. Nat Rev Cancer. 2016;16:413–30. [PubMed: 27282250]
3. Abelson S, Collord G, Ng SWK, Weissbrod O, Mendelson Cohen N, Niemeyer E, et al. Prediction of acute myeloid leukaemia risk in healthy individuals. Nature. 2018;559:400–4. [PubMed: 29988082]
4. Desai P, Mencia-Trinchant N, Savenkov O, Simon MS, Cheang G, Lee S, et al. Somatic mutations precede acute myeloid leukemia years before diagnosis. Nat Med. 2018;24:1015–23. [PubMed: 29988143]
5. Genovese G, Kahler AK, Handsaker RE, Lindberg J, Rose SA, Bakhoum SF, et al. Clonal hematopoiesis and blood-cancer risk inferred from blood DNA sequence. N Engl J Med. 2014;371:2477–87. [PubMed: 25426838]
6. Jaiswal S, Fontanillas P, Flannick J, Manning A, Grauman PV, Mar BG, et al. Age-related clonal hematopoiesis associated with adverse outcomes. N Engl J Med. 2014;371:2488–98. [PubMed: 25426837]
7. Yoshida K, Sanada M, Shiraishi Y, Nowak D, Nagata Y, Yamamoto R, et al. Frequent pathway mutations of splicing machinery in myelodysplasia. Nature. 2011;478:64–9. [PubMed: 21909114]
8. Papaemmanuil E, Cazzola M, Boultwood J, Malcovati L, Vyas P, Bowen D, et al. Somatic SF3B1 mutation in myelodysplasia with ring sideroblasts. N Engl J Med. 2011;365:1384–95. [PubMed: 21995386]
9. Graubert TA, Shen D, Ding L, Okeyo-Owuor T, Lunn CL, Shao J, et al. Recurrent mutations in the U2AF1 splicing factor in myelodysplastic syndromes. Nat Genet. 2011;44:53–7. [PubMed: 22158538]
10. Patel BJ, Przychodzen B, Thota S, Radivoyevitch T, Visconte V, Kuzmanovic T, et al. Genomic determinants of chronic myelomonocytic leukemia. Leukemia. 2017;31:2815–23. [PubMed: 28555081]
11. Chen S, Benbarche S, Abdel-Wahab O. Splicing factor mutations in hematologic malignancies. Blood. 2021;138:599–612. [PubMed: 34157091]
12. Nguyen HD, Yadav T, Giri S, Saez B, Graubert TA, Zou L. Functions of Replication Protein A as a Sensor of R Loops and a Regulator of RNaseH1. Mol Cell. 2017;65:832–847.e4. [PubMed: 28257700]
13. Nguyen HD, Leong WY, Li W, Reddy PNG, Sullivan JD, Walter MJ, et al. Spliceosome Mutations Induce R Loop-Associated Sensitivity to ATR Inhibition in Myelodysplastic Syndromes. Cancer Res. 2018;78:5363–74. [PubMed: 30054334]
14. Flach J, Jann J-C, Knaflic A, Riabov V, Streuer A, Altrock E, et al. Replication stress signaling is a therapeutic target in myelodysplastic syndromes with splicing factor mutations. Haematologica. 2021;106:2906–17. [PubMed: 33054116]
15. Chen L, Chen J-Y, Huang Y-J, Gu Y, Qiu J, Qian H, et al. The Augmented R-Loop Is a Unifying Mechanism for Myelodysplastic Syndromes Induced by High-Risk Splicing Factor Mutations. Mol Cell. 2018;69:412–425.e6. [PubMed: 29395063]
16. Singh S, Ahmed D, Dolatshad H, Tatwavedi D, Schulze U, Sanchi A, et al. SF3B1 mutations induce R-loop accumulation and DNA damage in MDS and leukemia cells with therapeutic implications. Leukemia. 2020;34:2525–30. [PubMed: 32076118]

17. Crossley MP, Bocek M, Cimprich KA. R-loops as cellular regulators and genomic threats. Mol Cell. 2019;73:398–411. [PubMed: 30735654]
18. Bhatia V, Herrera-Moyano E, Aguilera A, Gómez-González B. The role of replication-associated repair factors on R-Loops. Genes (Basel). 2017;8:E171.
19. Lee SC-W, Dvinge H, Kim E, Cho H, Micol J-B, Chung YR, et al. Modulation of splicing catalysis for therapeutic targeting of leukemia with mutations in genes encoding spliceosomal proteins. Nat Med. 2016;22:672–8. [PubMed: 27135740]
20. Shirai CL, White BS, Tripathi M, Tapia R, Ley JN, Ndonwi M, et al. Mutant U2AF1-expressing cells are sensitive to pharmacological modulation of the spliceosome. Nat Commun. 2017;8:14060. [PubMed: 28067246]
21. Fei DL, Motowski H, Chatrikhi R, Prasad S, Yu J, Gao S, et al. Wild-Type U2AF1 Antagonizes the Splicing Program Characteristic of U2AF1-Mutant Tumors and Is Required for Cell Survival. PLoS Genet. 2016;12:e1006384. [PubMed: 27776121]
22. Zhou Q, Derti A, Ruddy D, Rakiec D, Kao I, Lira M, et al. A chemical genetics approach for the functional assessment of novel cancer genes. Cancer Res. 2015;75:1949–58. [PubMed: 25788694]
23. Fong JY, Pignata L, Goy P-A, Kawabata KC, Lee SC-W, Koh CM, et al. Therapeutic Targeting of RNA Splicing Catalysis through Inhibition of Protein Arginine Methylation. Cancer Cell. 2019;36:194–209.e9. [PubMed: 31408619]
24. Obeng EA, Chappell RJ, Seiler M, Chen MC, Campagna DR, Schmidt PJ, et al. Physiologic Expression of Sf3b1(K700E) Causes Impaired Erythropoiesis, Aberrant Splicing, and Sensitivity to Therapeutic Spliceosome Modulation. Cancer Cell. 2016;30:404–17. [PubMed: 27622333]
25. Seiler M, Yoshimi A, Darman R, Chan B, Keaney G, Thomas M, et al. H3B-8800, an orally available small-molecule splicing modulator, induces lethality in spliceosome-mutant cancers. Nat Med. 2018;24:497–504. [PubMed: 29457796]
26. Wang E, Lu SX, Pastore A, Chen X, Imig J, Chun-Wei Lee S, et al. Targeting an RNA-Binding Protein Network in Acute Myeloid Leukemia. Cancer Cell. 2019;35:369–384.e7. [PubMed: 30799057]
27. Steensma DP, Wermke M, Klimek VM, Greenberg PL, Font P, Komrokji RS, et al. Phase I first-in-human dose escalation study of the oral SF3B1 modulator H3B-8800 in myeloid neoplasms. Leukemia. 2021;35:3542–50. [PubMed: 34172893]
28. Brunner AM, Liu Y, Mendez LM, Garcia JS, Amrein PC, Neuberg DS, et al. Inhibition of ATR with AZD6738 (Ceralasertib) for the treatment of progressive or relapsed myelodysplastic syndromes and chronic myelomonocytic leukemia: safety and preliminary activity from a phase Ib/II study. Blood. 2021;138:1521–1521.
29. Chatrikhi R, Feeney CF, Pulvino MJ, Alachouzos G, MacRae AJ, Falls Z, et al. A synthetic small molecule stalls pre-mRNA splicing by promoting an early-stage U2AF2-RNA complex. Cell Chemical Biology. 2021;28:1145–1157.e6. [PubMed: 33689684]
30. Hsu J, Reilly A, Hayes BJ, Clough CA, Konnick EQ, Torok-Storb B, et al. Reprogramming identifies functionally distinct stages of clonal evolution in myelodysplastic syndromes. Blood. 2019;134:186–98. [PubMed: 31010849]
31. Clough CA, Pangallo J, Sarchi M, Ilagan JO, North K, Bergantinos R, et al. Coordinated missplicing of TMEM14C and ABCB7 causes ring sideroblast formation in SF3B1-mutant myelodysplastic syndrome. Blood. 2022;139:2038–49. [PubMed: 34861039]
32. Kotini AG, Chang C-J, Boussaad I, Delrow JJ, Dolezal EK, Nagulapally AB, et al. Functional analysis of a chromosomal deletion associated with myelodysplastic syndromes using isogenic human induced pluripotent stem cells. Nat Biotechnol. 2015;33:646–55. [PubMed: 25798938]
33. Wheeler EC, Vora S, Mayer D, Kotini AG, Olszewska M, Park SS, et al. Integrative RNA-omics Discovers GNAS Alternative Splicing as a Phenotypic Driver of Splicing Factor-Mutant Neoplasms. Cancer Discov. 2022;12:836–55. [PubMed: 34620690]
34. Kim E, Ilagan JO, Liang Y, Daubner GM, Lee SC, Ramakrishnan A, et al. SRSF2 Mutations Contribute to Myelodysplasia by Mutant-Specific Effects on Exon Recognition. Cancer Cell. 2015;27:617–30. [PubMed: 25965569]

35. Fei DL, Zhen T, Durham B, Ferrarone J, Zhang T, Garrett L, et al. Impaired hematopoiesis and leukemia development in mice with a conditional knock-in allele of a mutant splicing factor gene U2af1. Proc Natl Acad Sci U S A. 2018;115:E10437–46. [PubMed: 30322915]
36. de Boer J, Williams A, Skavdis G, Harker N, Coles M, Tolaini M, et al. Transgenic mice with hematopoietic and lymphoid specific expression of Cre. Eur J Immunol. 2003;33:314–25. [PubMed: 12548562]
37. Kühn R, Schwenk F, Aguet M, Rajewsky K. Inducible gene targeting in mice. Science. 1995;269:1427–9. [PubMed: 7660125]
38. Fallahi-Sichani M, Honarnejad S, Heiser LM, Gray JW, Sorger PK. Metrics other than potency reveal systematic variation in responses to cancer drugs. Nat Chem Biol. 2013;9:708–14. [PubMed: 24013279]
39. Ritz C, Baty F, Streibig JC, Gerhard D. Dose-Response Analysis Using R. PLOS ONE. 2015;10:e0146021. [PubMed: 26717316]
40. Simoneau A, Xiong R, Zou L. The trans cell cycle effects of PARP inhibitors underlie their selectivity toward BRCA1/2-deficient cells. Genes Dev. 2021;35:1271–89. [PubMed: 34385259]
41. Laspata N, Kaur P, Mersaoui SY, Muoio D, Liu ZS, Bannister MH, et al. PARP1 associates with R-loops to promote their resolution and genome stability. Nucleic Acids Res. 2023;51:2215–37. [PubMed: 36794853]
42. Matos DA, Zhang J-M, Ouyang J, Nguyen HD, Genois M-M, Zou L. ATR protects the genome against R loops through a MUS81-triggered feedback loop. Mol Cell. 2020;77:514–527.e4. [PubMed: 31708417]
43. Weinstock DM, Nakanishi K, Helgadottir HR, Jasin M. Assaying double-strand break repair pathway choice in mammalian cells using a targeted endonuclease or the RAG recombinase. Methods Enzymol. 2006;409:524–40. [PubMed: 16793422]
44. Maifrede S, Le BV, Nieborowska-Skorska M, Golovine K, Sullivan-Reed K, Dunuwille WMB, et al. TET2 and DNMT3A Mutations Exert Divergent Effects on DNA Repair and Sensitivity of Leukemia Cells to PARP Inhibitors. Cancer Res. 2021;81:5089–101. [PubMed: 34215619]
45. Walsh T, Lee MK, Casadei S, Thornton AM, Stray SM, Pennil C, et al. Detection of inherited mutations for breast and ovarian cancer using genomic capture and massively parallel sequencing. Proc Natl Acad Sci U S A. 2010;107:12629–33. [PubMed: 20616022]
46. Norquist BM, Brady MF, Harrell MI, Walsh T, Lee MK, Gulsuner S, et al. Mutations in Homologous Recombination Genes and Outcomes in Ovarian Carcinoma Patients in GOG 218: An NRG Oncology/Gynecologic Oncology Group Study. Clin Cancer Res. 2018;24:777–83. [PubMed: 29191972]
47. Pennington KP, Walsh T, Harrell MI, Lee MK, Pennil CC, Rendi MH, et al. Germline and somatic mutations in homologous recombination genes predict platinum response and survival in ovarian, fallopian tube, and peritoneal carcinomas. Clin Cancer Res. 2014;20:764–75. [PubMed: 24240112]
48. Cunningham F, Allen JE, Allen J, Alvarez-Jarreta J, Amode MR, Armean IM, et al. Ensembl 2022. Nucleic Acids Res. 2022;50:D988–95. [PubMed: 34791404]
49. Patro R, Duggal G, Love MI, Irizarry RA, Kingsford C. Salmon provides fast and bias-aware quantification of transcript expression. Nat Methods. 2017;14:417–9. [PubMed: 28263959]
50. Love MI, Huber W, Anders S. Moderated estimation of fold change and dispersion for RNA-seq data with DESeq2. Genome Biol. 2014;15:550. [PubMed: 25516281]
51. Shen S, Park JW, Lu Z, Lin L, Henry MD, Wu YN, et al. rMATS: robust and flexible detection of differential alternative splicing from replicate RNA-Seq data. Proc Natl Acad Sci U S A. 2014;111:E5593–5601. [PubMed: 25480548]
52. Park JW, Tokheim C, Shen S, Xing Y. Identifying differential alternative splicing events from RNA sequencing data using RNASeq-MATS. Methods Mol Biol. 2013;1038:171–9. [PubMed: 23872975]
53. Shen S, Park JW, Huang J, Dittmar KA, Lu Z, Zhou Q, et al. MATS: a Bayesian framework for flexible detection of differential alternative splicing from RNA-Seq data. Nucleic Acids Res. 2012;40:e61. [PubMed: 22266656]

54. Kanehisa M, Goto S. KEGG: kyoto encyclopedia of genes and genomes. Nucleic Acids Res. 2000;28:27–30. [PubMed: 10592173]
55. Kanehisa M, Furumichi M, Sato Y, Kawashima M, Ishiguro-Watanabe M. KEGG for taxonomy-based analysis of pathways and genomes. Nucleic Acids Res. 2023;51:D587–92. [PubMed: 36300620]
56. Lavallée V-P, Baccelli I, Krosl J, Wilhelm B, Barabé F, Gendron P, et al. The transcriptomic landscape and directed chemical interrogation of MLL-rearranged acute myeloid leukemias. Nat Genet. 2015;47:1030–7. [PubMed: 26237430]
57. Lee SC-W, North K, Kim E, Jang E, Obeng E, Lu SX, et al. Synthetic Lethal and Convergent Biological Effects of Cancer-Associated Spliceosomal Gene Mutations. Cancer Cell. 2018;34:225–241.e8. [PubMed: 30107174]
58. Mateo J, Lord CJ, Serra V, Tutt A, Balmaña J, Castroviejo-Bermejo M, et al. A decade of clinical development of PARP inhibitors in perspective. Ann Oncol. 2019;30:1437–47. [PubMed: 31218365]
59. Buisson R, Niraj J, Rodrigue A, Ho CK, Kreuzer J, Foo TK, et al. Coupling of Homologous Recombination and the Checkpoint by ATR. Mol Cell. 2017;65:336–46. [PubMed: 28089683]
60. Arnoult N, Correia A, Ma J, Merlo A, Garcia-Gomez S, Maric M, et al. Regulation of DNA repair pathway choice in S and G2 phases by the NHEJ inhibitor CYREN. Nature. 2017;549:548–52. [PubMed: 28959974]
61. Lappin KM, Barros EM, Jhujh SS, Irwin GW, McMillan H, Liberante FG, et al. Cancer-Associated SF3B1 Mutations Confer a BRCA-Like Cellular Phenotype and Synthetic Lethality to PARP Inhibitors. Cancer Res. 2022;82:819–30. [PubMed: 35027467]
62. Bland P, Saville H, Wai PT, Curnow L, Muirhead G, Nieminuszczy J, et al. SF3B1 hotspot mutations confer sensitivity to PARP inhibition by eliciting a defective replication stress response. Nat Genet. 2023;55:1311–23. [PubMed: 37524790]
63. Kotake Y, Sagane K, Owa T, Mimori-Kiyosue Y, Shimizu H, Uesugi M, et al. Splicing factor SF3b as a target of the antitumor natural product pladienolide. Nat Chem Biol. 2007;3:570–5. [PubMed: 17643112]
64. Yokoi A, Kotake Y, Takahashi K, Kadowaki T, Matsumoto Y, Minoshima Y, et al. Biological validation that SF3b is a target of the antitumor macrolide pladienolide. FEBS J. 2011;278:4870–80. [PubMed: 21981285]
65. Wan Y, Zheng X, Chen H, Guo Y, Jiang H, He X, et al. Splicing function of mitotic regulators links R-loop-mediated DNA damage to tumor cell killing. J Cell Biol. 2015;209:235–46. [PubMed: 25918225]
66. Wahba L, Amon JD, Koshland D, Vuica-Ross M. RNase H and multiple RNA biogenesis factors cooperate to prevent RNA:DNA hybrids from generating genome instability. Mol Cell. 2011;44:978–88. [PubMed: 22195970]
67. Hamperl S, Bocek MJ, Saldivar JC, Swigut T, Cimprich KA. Transcription-replication conflict orientation modulates R-loop levels and activates distinct DNA damage responses. Cell. 2017;170:774–786.e19. [PubMed: 28802045]
68. Cristini A, Groh M, Kristiansen MS, Gromak N. RNA/DNA Hybrid Interactome Identifies DXH9 as a Molecular Player in Transcriptional Termination and R-Loop-Associated DNA Damage. Cell Rep. 2018;23:1891–905.
69. Ray Chaudhuri A, Nussenzweig A. The multifaceted roles of PARP1 in DNA repair and chromatin remodelling. Nat Rev Mol Cell Biol. 2017;18:610–21. [PubMed: 28676700]
70. Kim D-S, Challa S, Jones A, Kraus WL. PARPs and ADP-ribosylation in RNA biology: from RNA expression and processing to protein translation and proteostasis. Genes Dev. 2020;34:302–20. [PubMed: 32029452]
71. Wang IX, Grunseich C, Fox J, Burdick J, Zhu Z, Ravazian N, et al. Human proteins that interact with RNA/DNA hybrids. Genome Res. 2018;28:1405–14. [PubMed: 30108179]
72. Mosler T, Conte F, Longo GMC, Mikicic I, Kreim N, Möckel MM, et al. R-loop proximity proteomics identifies a role of DDX41 in transcription-associated genomic instability. Nat Commun. 2021;12:7314. [PubMed: 34916496]

73. Yan Q, Wulfridge P, Doherty J, Fernandez-Luna JL, Real PJ, Tang H-Y, et al. Proximity labeling identifies a repertoire of site-specific R-loop modulators. Nat Commun. 2022;13:53. [PubMed: 35013239]

74. Ayyappan V, Wat R, Barber C, Vivelo CA, Gauch K, Visanpattanasin P, et al. ADPriboDB 2.0: an updated database of ADP-ribosylated proteins. Nucleic Acids Res. 2021;49:D261–5. [PubMed: 33137182]

75. Sollier J, Stork CT, García-Rubio ML, Paulsen RD, Aguilera A, Cimprich KA. Transcription-coupled nucleotide excision repair factors promote R-loop-induced genome instability. Mol Cell. 2014;56:777–85. [PubMed: 25435140]

76. Molenaar RJ, Radivoyevitch T, Nagata Y, Khurshed M, Przychodzen B, Makishima H, et al. IDH1/2 mutations sensitize acute myeloid leukemia to PARP inhibition and this is reversed by IDH1/2-mutant inhibitors. Clin Cancer Res. 2018;24:1705–15. [PubMed: 29339439]

77. Tothova Z, Valton A-L, Gorelov RA, Vallurupalli M, Krill-Burger JM, Holmes A, et al. Cohesin mutations alter DNA damage repair and chromatin structure and create therapeutic vulnerabilities in MDS/AML. JCI Insight. 2021;6:e142149, 142149. [PubMed: 33351783]

78. Gbyli R, Song Y, Liu W, Gao Y, Biancon G, Chandhok NS, et al. In vivo anti-tumor effect of PARP inhibition in IDH1/2 mutant MDS/AML resistant to targeted inhibitors of mutant IDH1/2. Leukemia. 2022;1–11.

Statement of Significance

Spliceosome-mutant leukemias accumulate R-loops and require PARP1 to resolve transcription-replication conflicts and genomic instability, providing rationale to repurpose FDA-approved PARP inhibitors for patients carrying spliceosome gene mutations.

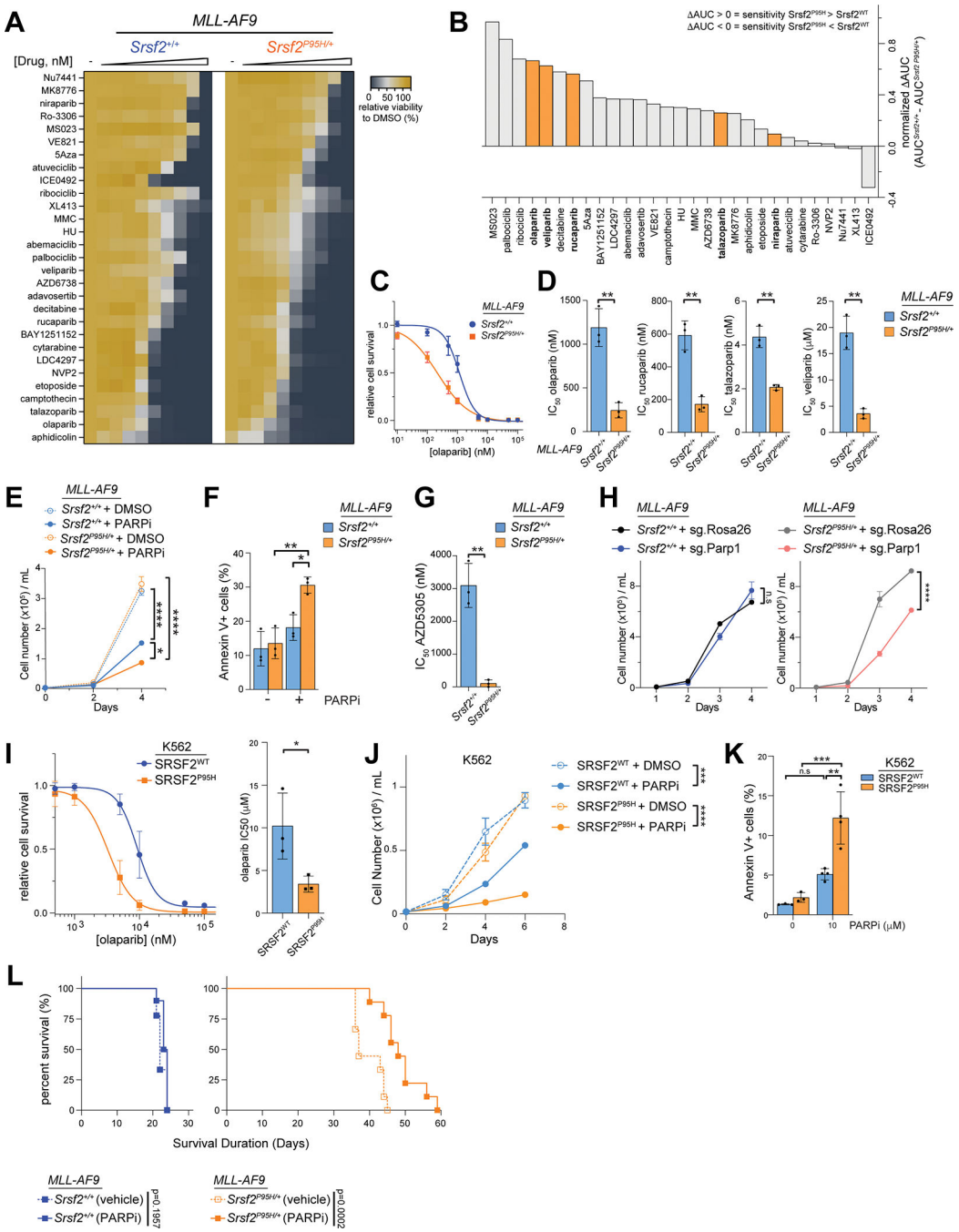

Figure 1. SRSF2-mutant leukemia confers sensitivity to PARP1/2 inhibitors.

(A-D) Murine *MLL-AF9 Srsf2*$^{+/+}$ and *MLL-AF9 Srsf2*$^{P95H/+}$ leukemia cells were treated either with DMSO (–) or a panel of pharmacologic inhibitors for 72 hours (n=3–4 independent experiments per inhibitor). Cell viability relative to DMSO was analyzed to generate relative viability heatmaps in (A); differential sensitivity analysis of indicated inhibitors based on normalized area under the curve (AUC) in (B); representative cell viability curve in response to olaparib in (C); and IC_{50} values for different PARP inhibitors (olaparib, rucaparib, talazoparib, veliparib) in the screen in (D). Statistical analysis was

performed using unpaired two-tailed Student's t-test (**, p<0.01). **(E)** *MLL-AF9 Srsf2*$^{+/+}$ and *MLL-AF9 Srsf2*$^{P95H/+}$ cells were treated with DMSO or PARPi (500 nM) for indicated days. Viable cell numbers were determined using trypan blue exclusion method. Error bars represent standard deviation (n=3 independent experiments). Statistical analysis using 2-way ANOVA was performed (*, **** indicate p<0.05, p<0.0001, respectively). **(F)** Cells were treated with DMSO or olaparib (PARPi; 1 μM) for 24h for Annexin V analysis. Error bars represent standard deviation (n=4 independent experiments). One-way analysis of variance (ANOVA) followed by Tukey's post-hoc test was used to adjust for multiple comparison (*, ** indicate p<0.05 and p<0.01, respectively). **(G)** IC_{50} of *MLL-AF9 Srsf2*$^{+/+}$ and *MLL-AF9 Srsf2*$^{P95H/+}$ cells for PARP1-specific inhibitor (AZD5305) treatment for 72 hours. Error bars represent standard deviation. Statistical analysis was performed using unpaired two-tailed Student's t-test (**, p<0.01). **(H)** *MLL-AF9 Srsf2*$^{+/+}$ and *MLL-AF9 Srsf2*$^{P95H/+}$ cells were genetically depleted of *Parp1* using CRISPR-Cas9. Viable cell numbers were determined using trypan blue exclusion method. Error bars represent standard deviation (n=3 independent experiments). Statistical analysis using 2-way ANOVA was performed (n.s. and **** indicate not significant and p<0.0001, respectively). **(I)** Relative cell viability, left, and IC_{50} values, right, of K562 *SRSF2*^{WT} and *SRSF2*^{P95H} cells in response to olaparib for 7 days (n=3–4 independent experiments). Statistical analysis was performed using unpaired two-tailed Student's t-test (*, p<0.05). **(J)** K562 *SRSF2*^{WT} and *SRSF2*^{P95H} cells were treated with either DMSO or PARPi (10 μM) for indicated days and viable cell number was determined using trypan blue exclusion method. Error bars represent standard deviation (n=3 independent experiments). Statistical analysis using 2-way ANOVA method was performed (***, **** indicate p<0.001, p<0.0001, respectively). **(K)** K562 SRSF2^{WT} and SRSF2^{P95H} cells were treated with DMSO or olaparib (10 μM, 24h) for Annexin V analysis. Error bars represent standard deviation (n=4 independent experiments). One-way ANOVA followed by Tukey's post-hoc test was used to adjust for multiple comparison (n.s., **, ***, indicate not significant, p<0.01, p<0.001, respectively). **(L)** Kaplan-Meier survival curves of mice transplanted with *MLL-AF9 Srsf2*$^{+/+}$ and *MLL-AF9 Srsf2*$^{P95H/+}$ leukemia cells followed by treatment with vehicle or PARPi (olaparib). The median survival time for each group: *MLL-AF9 Srsf2*$^{+/+}$ + vehicle (22 days; n=9 mice), *MLL-AF9 Srsf2*$^{+/+}$ + PARPi (23.5 days; n=10 mice), *MLL-AF9 Srsf2*$^{P95H/+}$ + vehicle (37 days; n=9 mice), *MLL-AF9 Srsf2*$^{P95H/+}$ + PARPi (48 days; n=9 mice). Mantel-Cox log-ranked test was used to compare differences in survival.

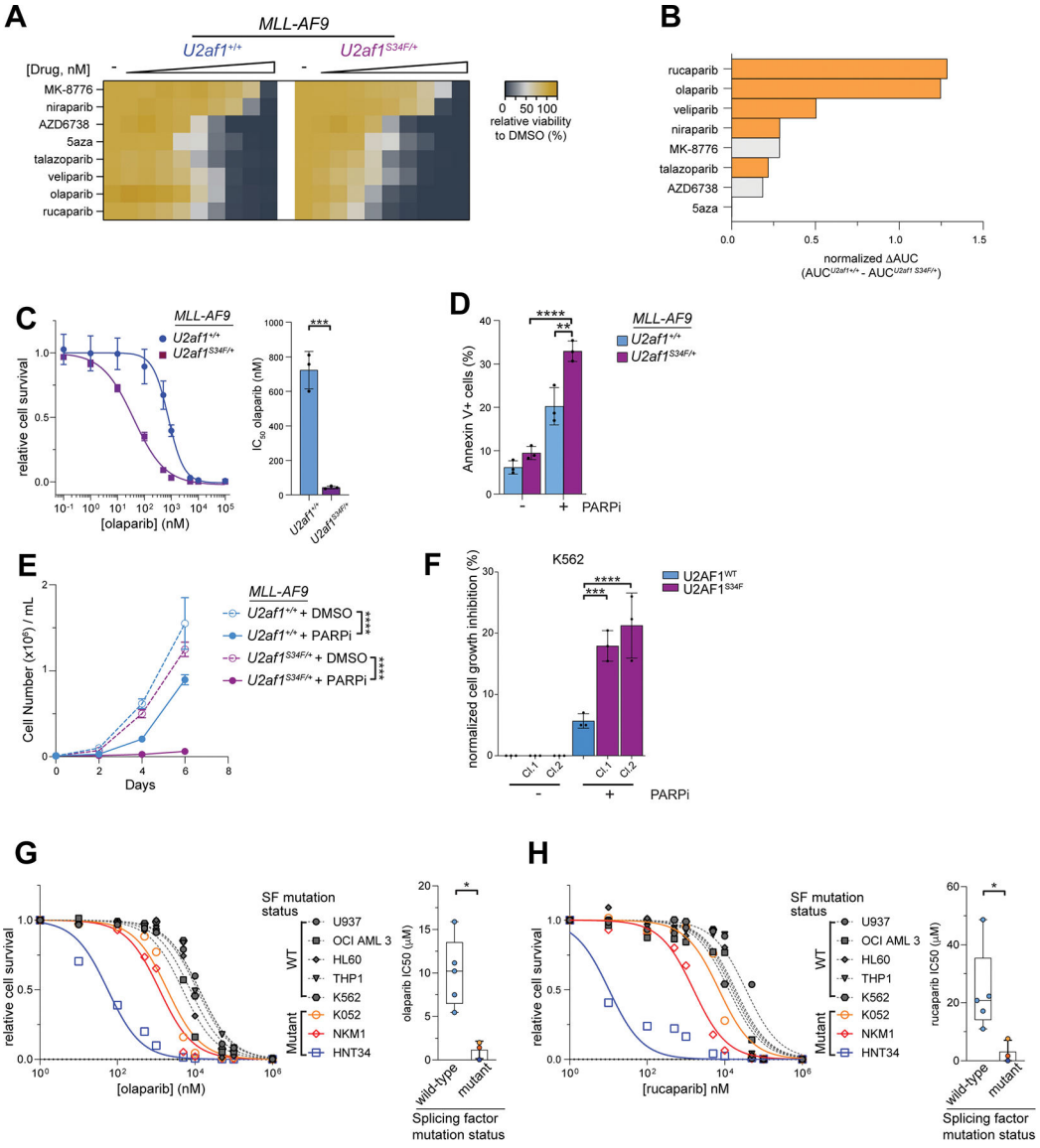

Figure 2. Spliceosome mutant leukemias confer sensitivity to PARP1/2 inhibitors.

(A-C) Murine *MLL-AF9 U2af1*$^{+/+}$ and *MLL-AF9* U*2af1*$^{S34F/+}$ leukemia cells were treated with either DMSO (–) or indicated pharmacologic inhibitors for 72 hours (n=3 independent experiments). Cell viability relative to DMSO was analyzed to generate relative viability heatmaps in (A); differential sensitivity analysis of indicated inhibitors based on normalized area under the curve (AUC) in (B); representative cell viability curve in response to olaparib in (C). Error bars represent standard deviation. Statistical analysis was performed using unpaired two-tailed Student's t-test (***, p<0.001). **(D)** Indicated murine cells were treated with DMSO or olaparib (PARPi; 1 μM) for 24 hours followed by Annexin V analysis. Error bars represent standard deviation (n=4 independent experiments). One-way analysis ANOVA followed by Tukey's post-hoc test was used to adjust for multiple comparison (**, ****, p<0.01, p<0.0001, respectively). **(E)** Cells were treated with DMSO or PARPi (500 nM) for indicated days. Viable cell numbers were determined using trypan blue exclusion method. Error bars represent standard deviation (n=3 independent experiments). Statistical

analysis using 2-way ANOVA was performed (****, $p<0.0001$). **(F)** Normalized cell growth inhibition of K562 $U2AF1^{WT}$ and $U2AF1^{S34F}$ cells. Error bars represent standard deviation (n=3 independent experiments). Statistical analysis was performed using unpaired two-tailed Student's t-test (***, ****, $p<0.001$, $p<0.0001$, respectively). **(G-H)** Relative cell viability and IC_{50} of indicated human leukemia cell lines that are either spliceosome wildtype or mutant were treated with olaparib (G) and rucaparib (H) for 7 days. Error bars represent standard deviation (n=3 independent experiments). Statistical analysis was performed using unpaired two-tailed Student's t-test (*, $p<0.05$).

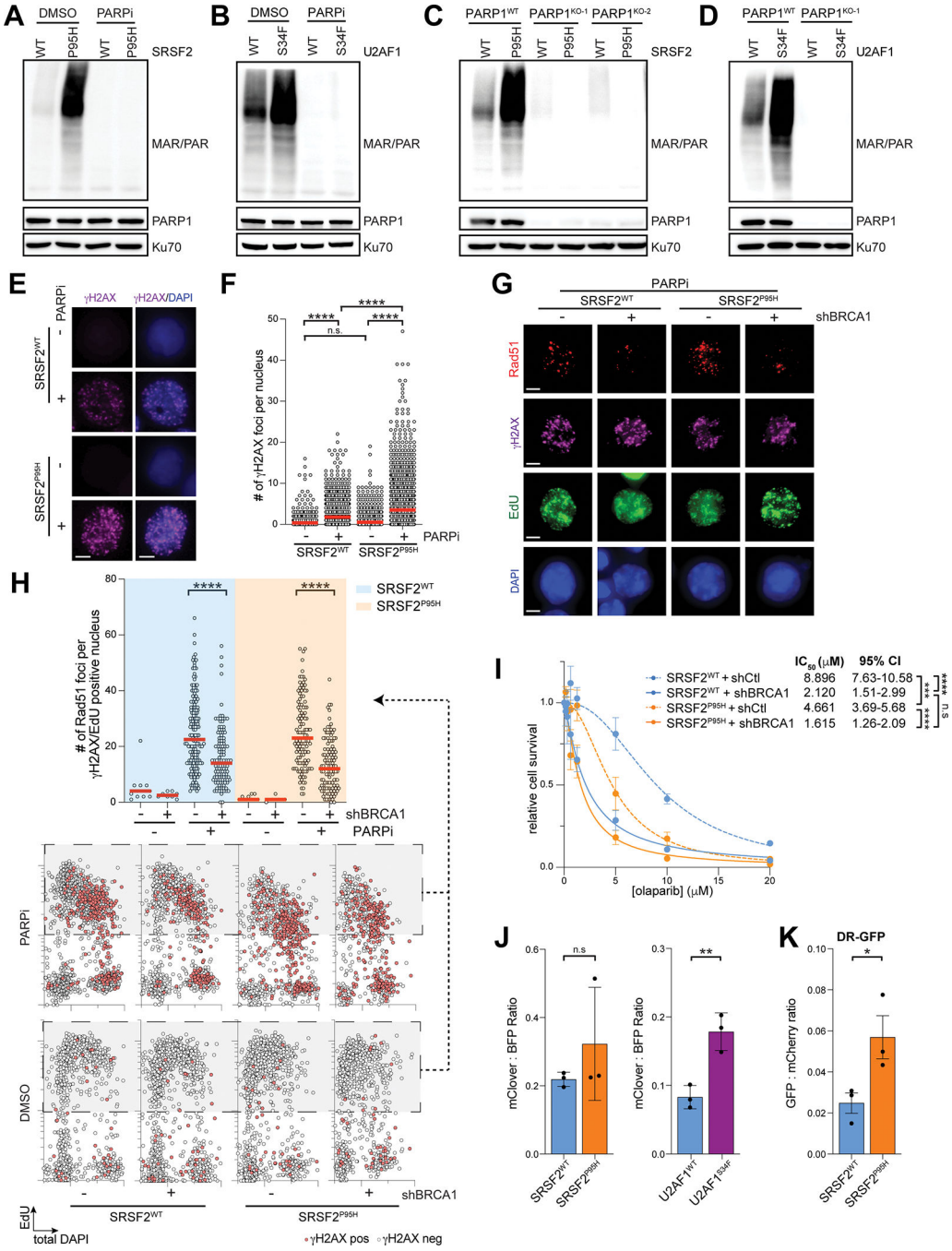

Figure 3. Increased PARP inhibitor sensitivity in spliceosome-mutant cells is HR-independent.

(A-B) Immunoblot analysis of total Mono-/poly-ADPribosylation (MAR/PAR) levels and PARP1 levels in K562 SRSF2^{WT} and SRSF2^{P95H} cells (A) and K562 U2AF1^{WT} and U2AF1^{S34F} cells (B) at steady state or following acute olaparib treatment (PARPi, 10 μM for 1 hour). **(C-D)** Assessment of total MAR/PAR levels following *PARP1* knockout in K562 SRSF2^{WT} and SRSF2^{P95H} cells (C) and in K562 U2AF1^{WT} and U2AF1^{S34F} cells (D). **(E-F)** K562 SRSF2^{WT} and SRSF2^{P95H} cells were treated with DMSO or olaparib (PARPi, 10 μM) for 24 hours for γH2AX immunofluorescence. Representative images and foci

number quantification per nucleus (n>2000) are shown in (E) and (F), respectively. Red bars represent the mean in the indicated groups. Statistical analysis was obtained using one-way ANOVA (****, p<0.0001, n.s., non-significant). **(G-H)** K562 SRSF2^{WT} and SRSF2^{P95H} cells expressing either shControl or shBRCA1 were treated with DMSO or olaparib (PARPi,10 μM for 24 hours). Representative images are shown in (G). In H, quantification of the Rad51 foci numbers per nucleus in EdU/γH2AX-double positive cells (n>110, top panel). Red bars represent the median in the indicated groups. Statistical analysis was done using ordinary one-way ANOVA (****, p<0.0001). Bottom, QBIC analysis of indicated cells treated with DMSO or olaparib. The gray boxes highlight EdU/γH2AX positive cells used for Rad51 analysis. **(I)** Relative cell viability of K562 SRSF2^{WT} and SRSF2^{P95H} cells expressing shControl (shCtl) or shBRCA1 cells treated with olaparib for 7 days. Error bars represent standard error of mean (n=9). Statistical analysis using two-way ANOVA was performed (***p<0.001, ****p<0.0001, n.s., non-significant). **(J)** Assessment of HR repair efficiency by mClover:BFP ratio in K562 SRSF2^{P95H} or U2AF1^{S34F} cells relative to their isogenic wildtype cells. Error bars represent standard deviation (n=3). Statistical analysis was performed using unpaired two-tailed Student's t-test (**p<0.01, n.s., non-significant). **(K)** Assessment of the HR repair function using the DR-GFP reporter cassette in K562 SRSF2^{WT} and SRSF2^{P95H} cells. Error bars represent standard deviation (n=3 independent experiments). Statistical analysis was performed using unpaired two-tailed Student's t-test (*, p<0.05).

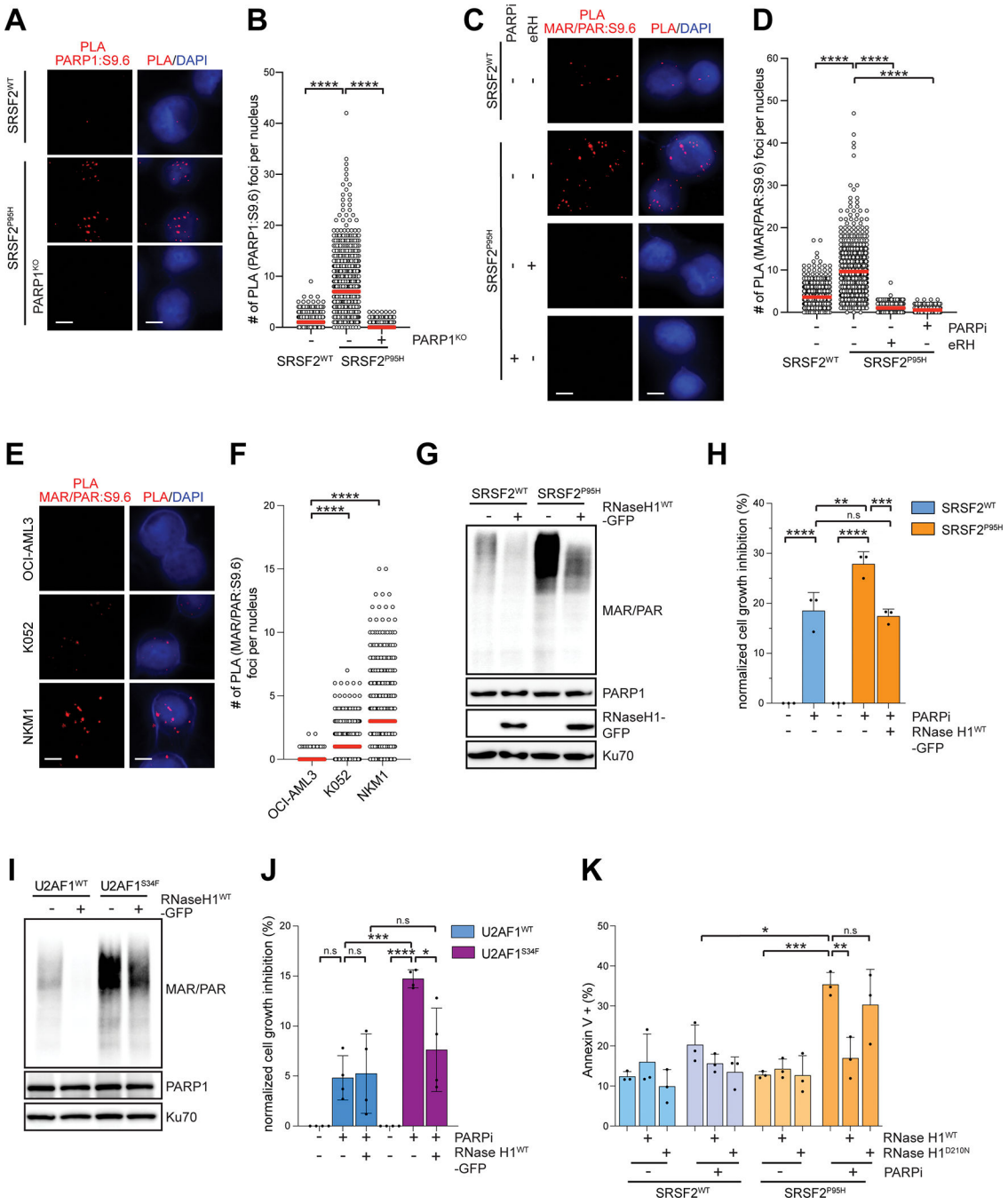

Figure 4. PARP1's activity at R loops in SF-mutant cells is critical to prevent PARPi-induced genomic instability.

(A) Representative images of S9.6:PARP1 PLA in indicated cells (scale bar = 5 μm). **(B)** Quantification of PLA foci numbers per nucleus in (A) (n>900). Red bars represent the median in the indicated groups. Statistical analysis was obtained using ordinary one-way ANOVA (****, p<0.0001). **(C)** Representative images of S9.6:MAR/PAR PLA in K562 SRSF2^{WT} and SRSF2^{P95H} cells treated with either acute olaparib (PARPi, 10 μM for 1h) treatment or *e.coli* RNase H (eRH) *in vitro* (scale bar = 5 μm). **(D)** Quantification of PLA

foci numbers per nucleus in (C) (n>500). Red bars represent the mean in the indicated groups. Statistical analysis was obtained using ordinary one-way ANOVA (****, p<0.0001). **(E)** Representative images of S9.6:MAR/PAR PLA foci in indicated cells, scale bar = 5 μm. **(F)** Quantification of PLA foci numbers per nucleus (n>500) for each condition in (E). Red bars represent the median in the indicated groups. Statistical analysis was obtained using ordinary one-way ANOVA (****, p<0.0001). **(G)** Immunoblot analysis of total MAR/PAR, PARP1 and GFP levels following doxycycline-inducible expression of nuclear, GFP-tagged RNase $H1^{WT}$ in K562 $SRSF2^{WT}$ and $SRSF2^{P95H}$ cells (100 ng/mL, 24 hours). **(H)** K562 $SRSF2^{WT}$ and $SRSF2^{P95H}$ cells inducibly expressing RNase $H1^{WT}$ (400 ng/mL dox) were treated with olaparib (PARPi, 5 μM) or DMSO for 3 days, and the cell growth was normalized to respective DMSO controls (n=3 independent experiments). Statistical analysis was performed using ordinary one-way ANOVA (**, ***, ****, n.s., indicate p<0.01, p<0.001, p<0.0001, non-significant, respectively). **(I)** Immunoblot analysis of total MAR/PAR and PARP1 levels following doxycycline-inducible expression of nuclear RNase $H1^{WT}$ in K562 $U2AF1^{WT}$ and $U2AF1^{S34F}$ cells (400 ng/mL dox, 24h). **(J)** K562 $U2AF1^{WT}$ and $U2AF1^{S34F}$ cells inducibly expressing nuclear RNase $H1^{WT}$ by addition of doxycycline (400 ng/mL) were treated with olaparib (PARPi, 5 μM) or DMSO for 5 days, and the cell growth was normalized to respective DMSO controls (n=3 independent experiments). Error bars represent standard deviation. Statistical analysis was performed using ordinary one-way ANOVA (*, **, ***, ****, n.s., indicate p<0.05, p<0.01, p<0.001, p<0.0001, non-significant, respectively). **(K)** RNase $H1^{WT}$ and RNase $H1^{D210N}$ were constitutively expressed in K562 $SRSF2^{WT}$ and $SRSF2^{P95H}$ cells and were treated with DMSO or olaparib (PARPi; 10 μM) for 24 hours followed by Annexin V analysis. Error bars represent standard deviation (n=3 independent experiments). Error bars represent standard deviation. Statistical analysis was performed using ordinary two-way ANOVA (*, **, ***, n.s., indicate p<0.05, p<0.01, p<0.001, non-significant, respectively).

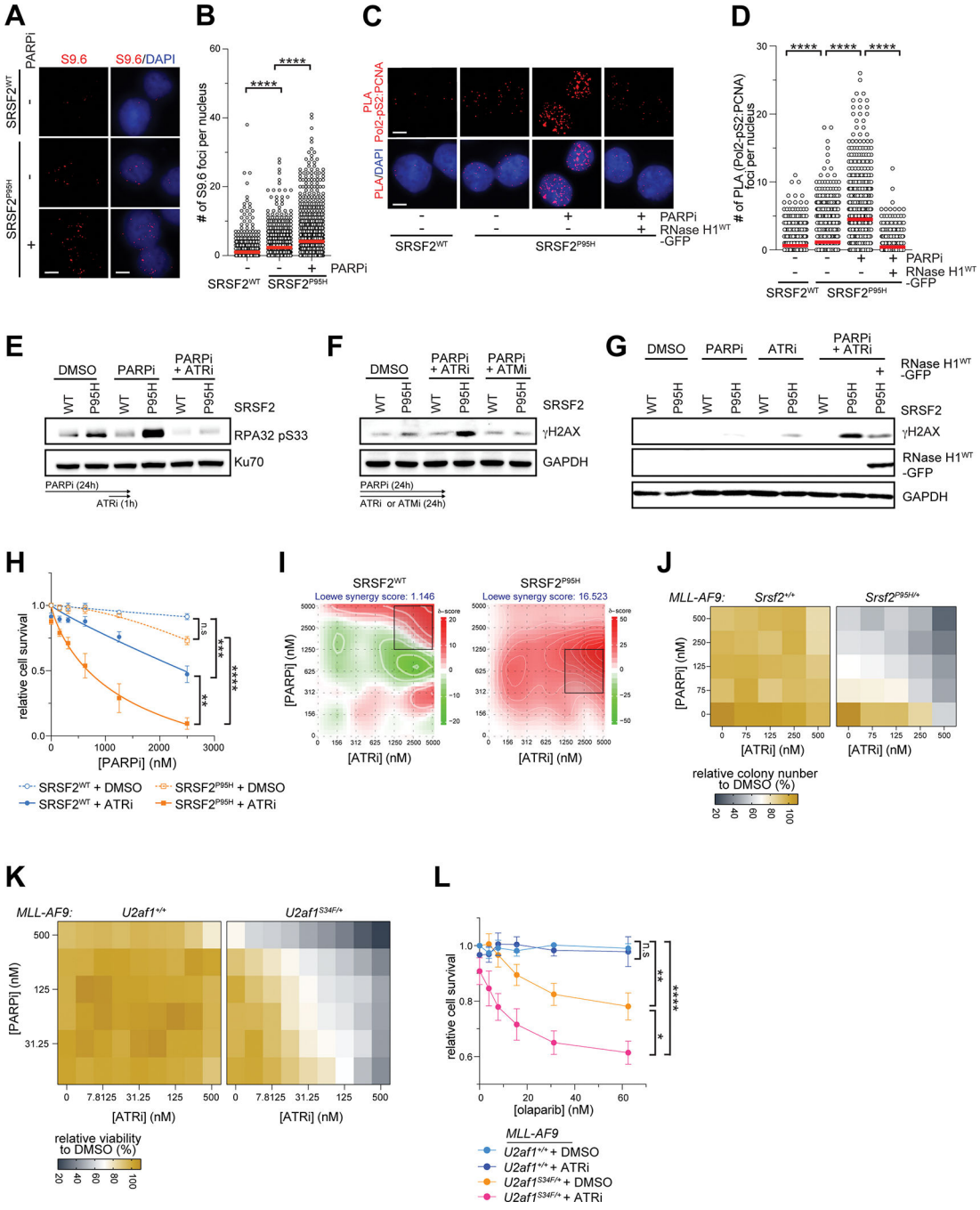

Figure 5. PARPi induces R-loop associated transcription-replication conflicts, rendering spliceosome-mutant cells more sensitive ATR inhibition.

(A-B) K562 SRSF2^{P95H} cells were treated with DMS or olaparib (PARPi, 3 μM) for 24h and subjected it S9.6 immunofluorescence. Representative images (scale bar = 5 μm) and quantification of S9.6 foci numbers per nucleus (n>1200) are shown in (A) and (B) respectively. Red bars represent the mean in the indicated groups. Statistical analysis was obtained using ordinary one-way ANOVA (****, p<0.0001, n.s., non-significant). **(C-D)** K562 SRSF2^{WT} and SRSF2^{P95H} cells were treated with DMSO or olaparib (PARPi, 3 μM)

for 24 hours. RNase H1-GFP expression in SRSF2^{P95H} cells was induced by addition of doxycycline (100 ng/mL). Representative images of RNA Pol2-pS2:PCNA PLA foci (scale bar = 5 μm) and quantification (n>650) are shown in (C) and (D), respectively. Red bars represent the mean in the indicated groups. Statistical analysis was obtained using one-way ANOVA (****, p<0.0001). **(E)** K562 SRSF2^{WT} and SRSF2^{P95H} cells were treated with DMSO, PARPi (olaparib, 3 μM) alone for 24 hours. ATR inhibitor (AZD6738, 10 μM) was added at the last 1 hour, followed by immunoblot analysis. **(F)** K562 SRSF2^{WT} and SRSF2^{P95H} cells were treated with PARPi+ATRi (3 μM each) or PARPi+ATMi (3 μM each) for 24 hours, followed by immunoblot analysis. **(G)** K562 SRSF2^{WT} and SRSF2^{P95H} cells were treated with either DMSO, olaparib (PARPi, 3 μM), or ATRi (AZD6738, 3 μM) alone, or combined PARP and ATR inhibitors for 24 hours. Doxycycline (200 ng/mL) was added in SRSF2^{P95H} cells to induce nuclear RNase H1^{WT} expression for the whole drug treatment duration. **(H)** Relative cell survival of K562 SRSF2^{WT} and SRSF2^{P95H} cells treated with either with DMSO or ATRi (AZD6738, 625 nM) and increasing concentrations of PARPi (olaparib) for 7 days. **(I)** Synergy maps for PARPi and ATRi combination treatment across six different doses for 4 days human K562 SRSF2^{WT} and SRSF2^{P95H} cells (n=3 independent experiments). Synergy score was determined using SynergyFinder 3.0. Loewe score >10 was considered as drug synergism downstream of R-loop response pathways. **(J)** Heatmaps showing the relative numbers of colony forming units in methylcellulose-containing media using murine *MLL-AF9* Srsf2^{WT} and *MLL-AF9* Srsf2^{P95H} cells following treatment with DMSO, or increasing concentrations of PARPi (olaparib), ATRi (AZD6738) alone or combined for 7 days (n=4 independent experiments). **(K)** Heatmaps showing the relative cell viability of murine *MLL-AF9* U2af1^{WT} and *MLL-AF9* U2af1^{S34F} leukemia cells treated with varying concentrations of individual PARPi (olaparib), ATRi (AZD6738) or combined for 72 hours (n=3 independent experiments). **(L)** Relative cell viability measured by CellTiterGlo from Fig. 5K using murine *MLL-AF9* U2af1^{WT} and U2af1^{S34F} leukemia cells treated either with DMSO or ATRi (AZD6738, 250 nM) and increasing concentrations of PARPi (olaparib) for 72 hours.

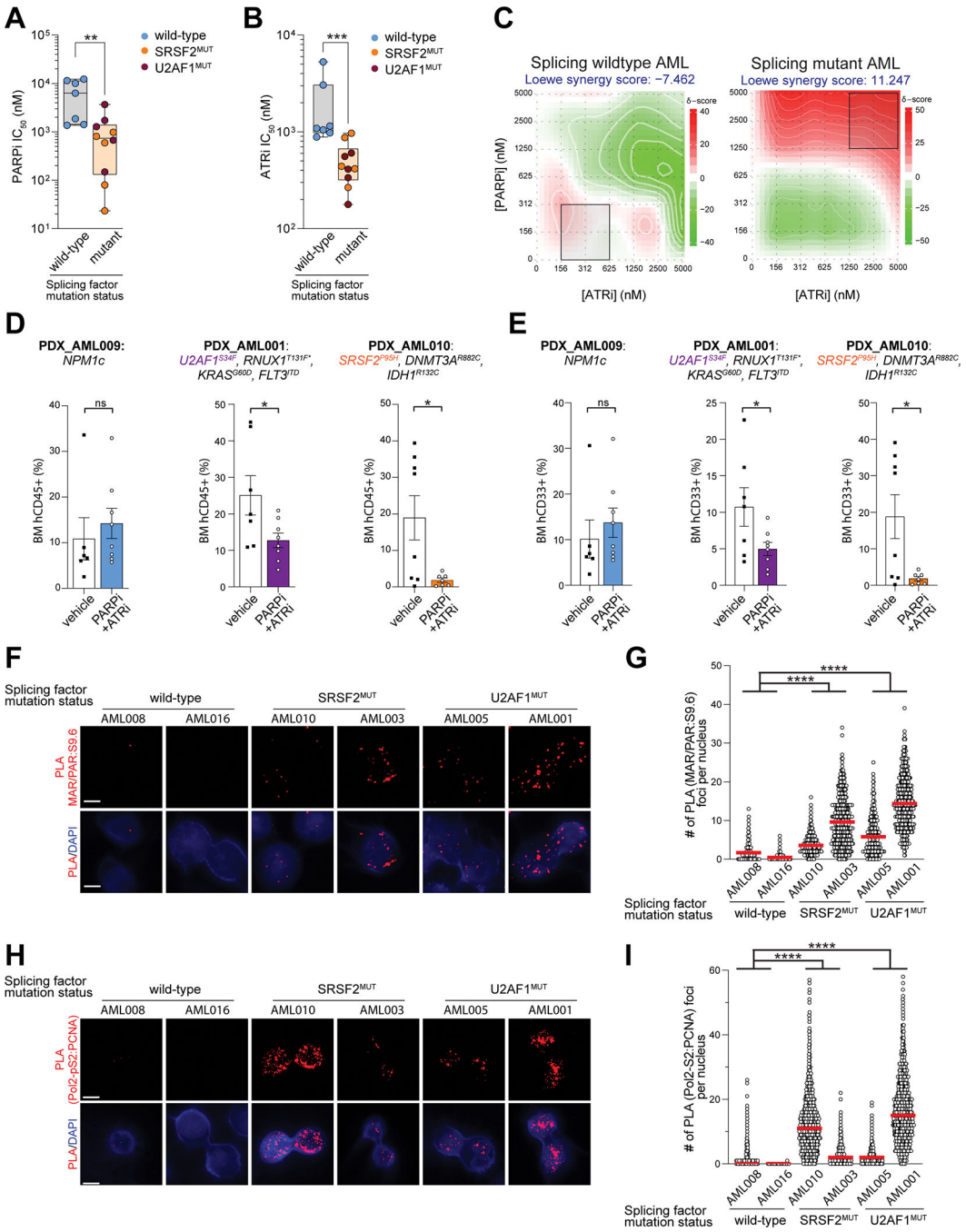

Figure 6. Primary human spliceosome mutant AML cells exhibited increased PARP1 activity at R loops and transcription-replication conflicts, rendering cells sensitive PARP and ATR inhibition *in vivo*.

(A-B). A total of n=7 spliceosome-wildtype and n=10 spliceosome-mutant (n=5 with an *SRSF2* mutation and n=5 with a *U2AF1* mutation) human primary acute myeloid leukemia (AML) patient samples were treated with PARPi and ATRi for 96 hours. See Supplementary Table S4 for detailed genetic information from each AML sample. The IC_{50} values for each drug are shown in (A and B). The top line of the whisker denotes the highest value in the dataset and the bottom line of the whisker denotes the lowest value. The box spans

the interquartile range (from 25th-75th percentile) and the line represents the median. Statistical analysis was performed using a two-tailed Mann-Whitney test (**, *** indicate $p<0.01$, $p<0.001$, respectively). **(C)** Synergy maps for combined PARP and ATR inhibition treatment for human primary AML cells. A total of n=4 splicing-wildtype and n=7 splicing mutants were used to determine the Loewe synergy score using SynergyFinder 3.0. **(D)** Bone marrow engraftment analysis of human $CD45^+$ cells in NSG-SGM3 mice in PDX models that were derived from patients that are either splicing wildtype or carry splicing factor mutations after treatment with vehicle or combination of olaparib and AZD6738 (PARPi+ATRi) for 6 weeks. **(E)** Bone marrow engraftment analysis of human $CD33^+$ cells in NSG-SGM3 mice in PDX models that were derived from patients that are either splicing wildtype or carry splicing factor mutation after treatment with vehicle or combination of olaparib and AZD6738 (PARPi+ATRi) for 6 weeks. Statistical analysis was performed using unpaired two-tailed Student's t-test (n.s., * indicate not significant and $p<0.05$, respectively). **(F)** Representative images of S9.6:MAR/PAR PLA in primary AML cells that are either splicing wildtype or carrying the splicing mutations. Scale bar = 5 μm. **(G)** Quantification of the number of S9.6:MAR/PAR PLA foci per nucleus (n>300) for each experimental condition illustrated in (F). Red bars represent the mean in the indicated groups. Statistical analysis was obtained using two-way ANOVA with Tukey's multiple comparisons test (****, $p<0.0001$). **(H)** Representative images of RNA Pol2-pS2:PCNA PLA in in primary AML cells that are either splicing wildtype or carry splicing mutations. Scale bar = 5 μm. **(I)** Quantification of the number of RNA Pol2-pS2:PCNA PLA foci per nucleus (n>500) for each condition in (H). Red bars represent the median in the indicated groups. Statistical analysis was obtained using two-way ANOVA with Tukey's multiple comparisons test (****, $p<0.0001$).

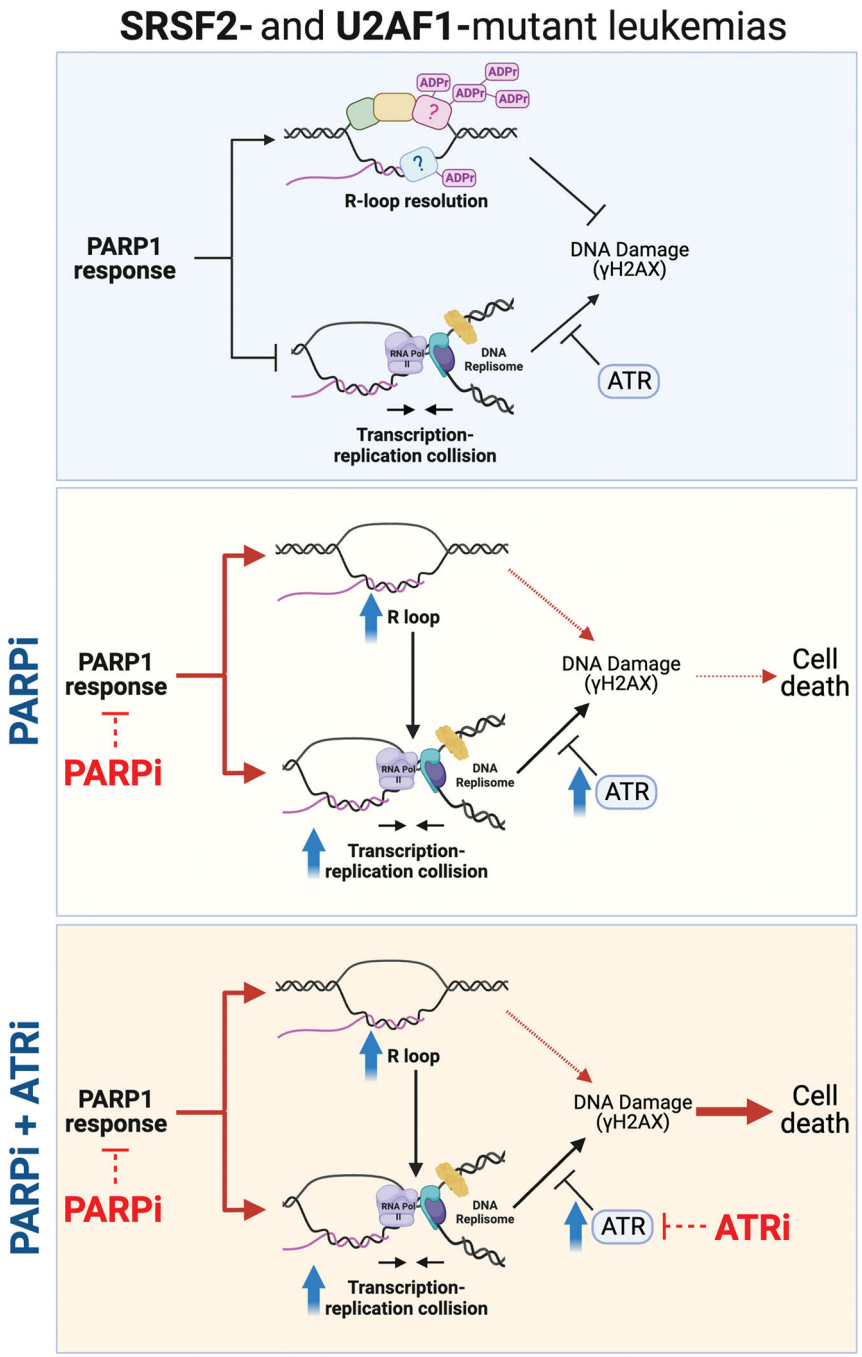

Figure 7. Proposed model for PARP1 function as a sensor of R loops in preventing transcription-replication conflicts in SF-mutant leukemias.

SRSF2- and U2AF1-mutant leukemias exhibited R-loop accumulation, causing transcription-replication conflicts. PARP1 senses and mediates ADP-ribosylation at R loops to prevent R-loop-induced genomic instability (top). In the presence of PARPi (middle), PARP1 is inactive and accumulates further R loops in SF-mutant cells. Aberrant R-loop accumulation causes more transcription-replication conflicts, leading to enhanced ATR

response (bottom). Consequently, combining PARP and ATR inhibitors synergistically kill SF-mutant leukemias.